REPORT DOCUMENTATION PAGE

AFRL-SR-AR-TR-09-0264

1. REPORT DATE *(DD-MM-YYYY)*	2. REPORT TYPE	3. DATES COVERED *(From - To)*
14-08-2009	Final Report	03/15/2006-05/31/2009

4. TITLE AND SUBTITLE

A Hierarchical Multiscale Particle Computational Method for Simulation of Nanoscale Flows on 3D Unstructured Grids

5a. CONTRACT NUMBER

5b. GRANT NUMBER
FA9950-06-1-0236

5c. PROGRAM ELEMENT NUMBER

6. AUTHOR(S)

Nikolaos A. Gatsonis

5d. PROJECT NUMBER

5e. TASK NUMBER

5f. WORK UNIT NUMBER

7. PERFORMING ORGANIZATION NAME(S) AND ADDRESS(ES)

Worcester Polytechnic Institute
100 Institute Rd.
Worcester, MA, 01609

8. PERFORMING ORGANIZATION REPORT NUMBER

9. SPONSORING / MONITORING AGENCY NAME(S) AND ADDRESS(ES)

AFOSR /NL
875 N. Randolph Street
Suite 325, RM 3112
Arlington, VA 22203
Dr Fariba Fahroo

10. SPONSOR/MONITOR'S ACRONYM(S)

11. SPONSOR/MONITOR'S REPORT NUMBER(S)

12. DISTRIBUTION / AVAILABILITY STATEMENT

Unlimited - Distribution A: Approved for Public Release

13. SUPPLEMENTARY NOTES

14. ABSTRACT

This research addresses mathematical and computational issues of particle methods for the three-dimensional simulation of flows at the nanoscale. The research addresses also the multi-scale physical phenomena in nanoscale flows that can be found in micro/nano fluidic devices and processes. The developments of an unstructured 3D Direct Simulation Monte Carlo (U3DSMC) method are presented, including a methodology for subsonic boundary conditions as well as the analysis of statistical fluctuations and errors in sample-averaged macroscopic flow properties obtained from U3DSMC simulations. The effects of number of samples, computational particles in a Delaunay cell, and Mach number on statistical fluctuations are investigated for uniform and pressure-driven nanoscale flows. A parametric investigation of supersonic flows into nanochannels examines the effects of Knudsen number, aspect ratio, and freestream Mach number. The computational implementation of a three-dimensional smooth dissipative particle dynamics method is presented along with a new solid-wall boundary condition methodology. Simulations of pressure driven flows show minimal density fluctuations in the proximity of walls and a good agreement with analytical results.

15. SUBJECT TERMS

Particle methods; DSMC; dissipative particle dynamics; nanoflow; microflow

16. SECURITY CLASSIFICATION OF:			17. LIMITATION OF ABSTRACT	18. NUMBER OF PAGES	19a. NAME OF RESPONSIBLE PERSON
a. REPORT	b. ABSTRACT	c. THIS PAGE			Nikolaos A. Gatsonis
Unlimited	Unlimited	Unlimited	Unlimited	39	19b. TELEPHONE NUMBER *(include area code)* 508-831-5576

SUMMARY

The emerging field of nanofluidics has significance to the Air Force with application to nanopropulsion, nano-rheology, nano-lubrication, control of nanosurface properties and lab-on-a-chip technologies. Biological and manufacturing processes that involve fluidic transport through nanoscale membranes and channels are also of significance to the Air Force. Design and operation of fluidic nanodevices as well as prediction and optimization of nanofluidic processes require proper mathematical and computational discretization. Modeling and simulation at the nanoscale (mesoscopic) range requires new mathematical and computational methods because the traditional atomistic (microscopic) and hydrodynamic (macroscopic) descriptions are not valid for either computational or theoretical reasons. The goals of research performed under FA9550-06-1-0236 were to:

- Develop the theoretical and numerical modeling of fluid flow at the nanoscale (mesoscopic) range.
- Address new multi length-scale, multi time-scale phenomena, and solid wall-fluid interactions that arise at the nanoscale.
- Investigate fluidic systems that incorporate geometries, fluids, and surface materials that are representative of nanodevices or nanoprocesses of interest to the Air Force.

The Objectives of the research performed under FA9550-06-1-0236 were to:

- Develop advanced particle computational methods for micro- and nano-scale flows.
- Develop numerical boundary conditions.
- Validate the numerical methods and evaluate their numerical errors.
- Investigate flows in nanochannels with length scales from 10 nm to 1000 nm.

We followed two distinct but inter-related Technical Approaches under FA9550-06-1-0236:

1) Further developed the unstructured DSMC (U3DSMC) method and code, originally developed by the PI under a previous AFOSR Grant F49620-03-1-0219. The new computational developments during this performance period allow:
   a) high-fidelity, gaseous nanoscale simulations;
   b) evaluation of error and uncertainty in DSMC nanoscale simulations; and,
   c) comparisons with results from the multiscale Dissipative Particle Dynamics (DPD) simulations.
2) Developed a hierarchical, multiscale, top-down approach from the Smoothed Particle Hydrodynamics (SPH) to Smoothed Dissipative Particle Dynamics (SDPD) that allows:
   a) computation of gaseous, liquid, and complex nanoflows;
   b) a two-level (SDPD/SPH) discretization of a mesoscale flow system by changing the character of the particle-particle interactions in order to move down the temporal-spatial scales.

The Mathematical and Computational Accomplishments of the U3DSMC approach are:

1. Explored computational issues that arise in the DSMC computation of nanoscale flows.
2. Developed the mathematical formulation and implemented a method for inflow and outflow boundary conditions in U3DSMC based on theory of characteristics.
3. Evaluated the numerical uncertainty and statistical fluctuations in macroscopic flow properties obtained from U3DSMC computations at the nanoscale. The statistical error in number density, mean velocity and translational temperature obtained from U3DSMC simulations was compared with theoretical estimates. The investigation considered the effects of the number of computational particles per Delaunay cell and Mach number on the fractional error for uniform and the pressure driven nanoflows.
4. Performed validation and grid sensitivity analysis of the U3DSMC method at the nanoscale:
    a. Compared U3DSMC simulations of supersonic flows into microchannels with 2D DSMC simulations.
    b. Compared heat transfer rates obtained with the U3DSMC method at the upper wall of a nanochannel with theoretical estimates applicable to the free-molecular regime.
    c. Compared mass flux at the outlet of a nanochannel with the results from the semi-analytical theory developed for free-molecular tube flows.
    d. Performed a grid sensitivity analysis for the U3DSMC method with simulations involving flows into nanochannels.
5. Applied U3DSMC to explore physical phenomena in supersonic sub-atmospheric and atmospheric gas flows into nanochannels and established the applicability of U3DSMC at the nanoscale.

The Mathematical and Computational Accomplishments of the SDPD approach are:

1. Initiated the development and computational implementation of a hierarchical, multiscale three-dimensional computational method that integrates the smooth dissipative particle dynamics and smooth particle hydrodynamic techniques.
2. Developed a new method for SDPD solid-wall boundary conditions.
3. Performed preliminary validation of the SDPD method.

1 UNSTRUCTURED 3D DIRECT SIMULATION MONTE CARLO (U3DSMC) METHOD FOR NANOSCALE COMPUTATIONS

We review below the elements of the U3DSMC method developed under FA9550-06-1-0236. We summarize also the numerical challenges associated with the DSMC simulations of nanoscale physical domains. Several basic algorithmic modules of U3DSCM, such as loading, injection, particle-tracing, and sampling of macroscopic variables, were developed by the PI under the previous AFOSR Grant F49620-03-1-0219 and are also shared by the unstructured particle in cell a methodology (U3dPIC) developed by Gatsonis and Spirkin (2009)[1] for the simulation of fully ionized flows. The new developments accomplished during 3/20006-5/2009 encompass the mathematical and computational aspects of the U3DSMC particle approach for high-fidelity gaseous nanoscale simulations. These developments appear in Chamberlin (2007)[2], Al-Khouz (2009)[3] and Gatsonis and Al-Khouz (2008)[4]. The U3DSMC code has also been applied to the simulation of gaseous expansion from micronozzles (Chamberlin and Gatsonis, 2007)[5] and the simulation of microscale jets (Chamberlin and Gatsonis, 2008)[6].

1.1 Computational Issues of DSMC for Nanoscale Flows

The increasing proliferation of MEMS devices as well as the design of NEMS devices and sensors that process gases, requires modeling and analysis of flows in nanoscale (or submicron) channels. The physical and the DSMC computational aspects of nanoflows have not been addressed so far and have some unique features. The computational of domains of interested are characterized by a scale $L \simeq 100 - 1000$ nm presents two challenges to the implementation of the DSMC method.

The first challenge relates to the small number of real particles present in a nanoscale domain. Figure 1 depicts the real number of particles in a domain with volume L^3, and number density in the range of $n_0 = 2.688 \times 10^{25}$ m^{-3} (at 1 atm) down to $0.01\, n_0$. The number of particles for $L \simeq 100$ nm decrease from $N \approx 10^4$ at n_0 to $N \approx 10^2$ at $0.01\, n_0$. For $L \simeq 1000$ nm the number of particles becomes $N \approx 10^7$ at n_0 and reduces to $N \approx 10^5$ at $0.01 n_0$. It is clear, that a DSMC computation of a nanoscale domain L^3 may require particle weights that are much smaller when compared with those used traditionally in micro- or macroscale applications, resulting in even fewer computational particles in the domain. The statistical fluctuations in sampled properties inherent to microflows[7] is expected to be more important to nanoflows.[2, 3] The accuracy of the computational parameters used in the nanoscale simulations (e.g. particle weights, cell-sizing, and time-steps) was verified with a grid sensitivity study and comparisons of the U3DSMC results with theoretical estimates.

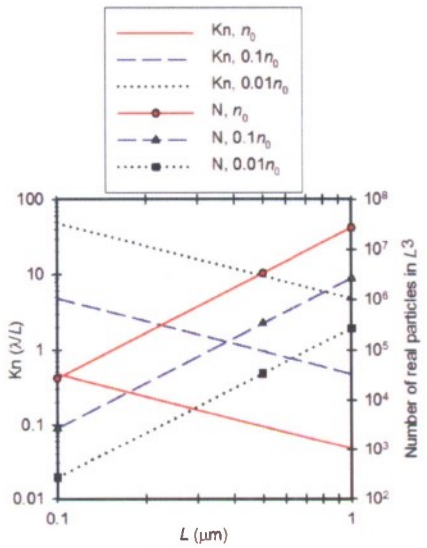

Figure 1. The Knudsen number as function of nanoscale length L and the number of real particles in a volume L^3. The standard number density n_0=2.69x10^{25} m^{-3}.

The second challenge relates to large Knudsen numbers associated with nanoflows. Figure 1 shows that for $L \simeq 100 - 1000\,\text{nm}$ a flow is expected to be in the transitional to free-molecular regime for all densities considered. Even under atmospheric pressure conditions (density of n_0) the $Kn \geq 0.05$. While transitional to near-free molecular conditions are often encountered in rarefied microscale or macroscale flows, it is also the case that their computational cells contain a large number of particles. At the nanoscale, the entire domain of interest characterized by L, can be of the order or smaller than λ. A DSMC simulation of a nanodomain, therefore, requires discretization with computational cells that can be of the same order as the entire domain with a small number of real particles residing into it. Furthermore, the number of sampling cells used for the evaluation of macroscopic fluid variables, such as density, mean velocity, temperature, may not be sufficient large to provide meaningful spatial resolution in a nanodomain. As a result, flow analysis requires the use of kinetic properties, such as the phase-space distributions, rather than macroscopic properties.

1.2 Unstructured 3D DSMC Method

The U3DSMC method is implemented on an unstructured, tetrahedral Delaunay mesh (Chamberlin, 2007). The grid generator discretizes the domain Ω by G_D Delaunay tetrahedra that have edge lengths scaling with a fraction of the local mean-free path, λ. Each node d is associated with the Voronoi dual, Γ_d, and the Delaunay supercell Ω_d formed by all the Delaunay cells that share the node d as illustrated in Figure 2 for a 2d geometry.

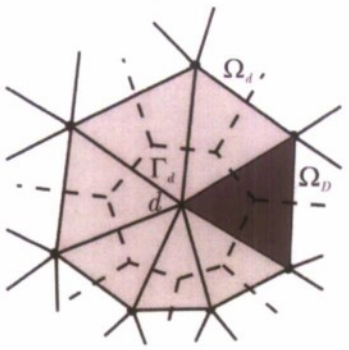

Figure 2. Grid structure used in the U3DSMC depicted in 2D for clarity. The Delaunay cell Ω_D, the Voronoi dual Γ_d, and a Delaunay supercell Ω_d and a node *d*.

1.2.1 *Particle Loading and Injection*

A number of computational particles, each representing F_W real particles, is loaded in the domain and injected from boundaries. In U3DSMC, particle loading is carried out by placing species s particles in each Delaunay cell with randomly chosen positions and velocities following the quasi-equilibrium, drifting Maxwellian distribution

$$f_{0s}(\mathbf{r},\mathbf{v},t) = n_s(\mathbf{r},t)\left(\frac{m_s}{2\pi k T_s}\right)^{3/2} \exp\left[-\frac{m_s(\mathbf{v}-\mathbf{V}_s)^2}{2kT_s}\right] \tag{1}$$

where number density $n_s(\mathbf{r},t)$, translational temperature $T_s(\mathbf{r},t)$, and mean species velocity $\mathbf{V}_s(\mathbf{r},t)$ are given. The number of computational particles loaded at each Delaunay cell is

$$N_{sD} = n_s(r,t)\Omega_D / F_W \tag{2}$$

where F_W is the particle weight. Computational particles are injected inside the domain from its boundaries. The inward flux of species s real particles across a Delaunay boundary surface is due to a drifting Maxwellian eq. (1)

$$\dot{\mathrm{N}}_s = \frac{n_s C_s^m}{2\sqrt{\pi}}\left(\exp\left(-S_s^2\cos^2(\theta)\right) + \sqrt{\pi}\, S_s \cos(\theta)\left\{1+\mathrm{erf}\left(S_s\cos(\theta)\right)\right\}\right), \tag{3}$$

where the most probable thermal speed is

$$C_s^m = \sqrt{2k_B T_s / m_s} \tag{4}$$

the mean velocity $\mathbf{V}_s$ is inclined at an angle θ to the unit normal vector $\mathbf{e}$. The speed ratio of the mean speed to the most probable speed is

$$S_s = V_s / C_c^m \tag{5}$$

The number of species s computational particles ΔN_s to be injected to the domain in a given time step, is

$$\Delta N_s = \dot{N}_s \Delta\tau \, A_s / F_W \,, \tag{6}$$

where $\Delta\tau$ is the time step and A_s is the area of the surface element.

1.2.2 *Integration of Particle Motion and Search for Particle Location*

The computational particles are tracked as they interact with other particles and with domain boundaries. For a particle p with position $\mathbf{r}_p(t)$ and velocity $\mathbf{v}_p(t) = (v_{px}, v_{py}, v_{pz})$ the new particle position is obtained from integration of the equation of motion, given by $\mathbf{r}_p(t+dt) = \mathbf{r}_p(t) + \mathbf{v}_p(t)\Delta\tau$. Tracing the motion of the particle on the unstructured grid is carried out using the successive-neighbor search algorithm (Gatsonis and Spirkin, 2008)[1]. In U3DSMC molecular motion over the time step ($\Delta\tau$) and intermolecular collisions occurring at a mean collision time, τ, are uncoupled, by choosing $\Delta\tau < \tau$.

1.2.3 *Elastic and Inelastic Collisions*

The selection of collision partners is performed within each Delaunay cell and follows Bird's no-time-counter (NTC) scheme.[8] The cross-section for elastic collisions is based on the variable hard sphere model (VHS). The Larsen-Borgnakke model is used to simulate the exchange of rotational energy between the collision pair.[9] Solid surfaces are modeled as being diffuse, non-diffuse or specularly reflecting. (Chamberlin, 2007)[2]

1.2.4 *Inflow and Outflow Boundary Conditions*

Inlet and outlet boundary conditions implemented in U3DSMC can accommodate supersonic and subsonic flows. For supersonic flows particles are injected using eq. (6) based on specified $n_s(\mathbf{r},t)$, $T_s(\mathbf{r},t)$, and $\mathbf{V}_s(\mathbf{r},t)$. The subsonic boundary method implemented in U3DSMC follows an approach that is based on the method of characteristics used in compressible flow computations. Similar methods have been used in 2D DSMC subsonic simulations (Nance et al., 1997;[10] Liou and Fang, 2000;[11] Wang and Li, 2004[12]). Our method was generalized to 3d unstructured grids and was supplemented with a neighboring-cell sampling approach and a smoothing technique to speed convergence. We followed Hirsch (1995)[13] and Yee at al. (1982)[14] and derived the boundary methodology implemented in U3DSMC. At a subsonic inflow boundary, the characteristic variables w_1, w_2 represent the physical boundary conditions, while at a subsonic outflow, w_3 is the physical boundary condition. For a subsonic inlet the two physical boundary conditions specified at the boundary are

p_1 and ρ_1. Zero-order space and zero-order time extrapolation of the characteristic variable w_3 between the boundary point and the interior point provides the numerical boundary condition and allows the evaluation of the third primitive variable, V_1. For a subsonic outlet designated by subscript M, w_3 is the physical boundary condition and the pressure is fixed at p_M. Zero-order space and zero-order time extrapolation of the characteristic variables and use of the numerical boundary conditions, provide the two primitive variables ρ_M and V_M. Once $n, T, \mathbf{V}$ are obtained on an inlet or outlet surface, the particles are injected into the domain following the injection procedure of eq. (6).

1.2.5 *Sampling and Macroscopic Flow Properties*

In U3DSMC macroscopic, single-fluid and multi-fluid variables, such as density, mean velocity, etc, are evaluated on nodes by averaging the particle properties within the Delaunay supercell Ω_d or the Voronoi cell Γ_d shown in Figure 2. For $N_{sD}(t)$ computational particles of species s residing in the sampling Delaunay cell with volume Ω_D the number density is defined as

$$n_s(D,t) \equiv \sum_{p=1}^{N_{sD}} F_{Wp} \Big/ \Omega_D \,, \tag{7}$$

the mean species velocity of the cell $\mathbf{V}_s(D,t) = \{V_{sx}, V_{sy}, V_{sz}\}$ is

$$\mathbf{V}_s(D,t) \equiv \sum_{p=1}^{N_{sD}} \mathbf{v}_{sp} \Big/ N_{sD} \,, \tag{8}$$

and the mass-average velocity of the cell $\mathbf{V}(D,t) = \{V_x, V_y, V_z\}$ is

$$\mathbf{V}(D,t) = \sum_s n_s m_s \mathbf{V}_s(D,t) \Big/ \sum_s n_s m_s \tag{9}$$

The thermal velocity $\mathbf{C}_{sp}$ is defined with respect to the mass-average velocity $\mathbf{V}$ as

$$\mathbf{C}_{sp} = \mathbf{v}_{sp} - \mathbf{V} \tag{10}$$

The translational temperature is

$$\frac{3}{2} k T_s(D,t) = \frac{1}{2} m_s \left(\sum_{p=1}^{N_{sD}} C_{sp}^2 \right) / N_{sD} \,, \tag{11}$$

and the scalar pressure is

$$p_s(D,t) = n_s(D,t) k T_s(D,t) \,. \tag{12}$$

We also calculate the overall single-fluid cell properties as

$$T(D,t) = \sum_s n_s T_s^*(D,t) \Big/ \sum_s n_s(D,t) \tag{13}$$

$$p(D,t) = \sum_{s} p_s^* \tag{14}$$

In addition to such cell-averaged properties the instantaneous value of any macroscopic variable $X(d,t) \equiv n(d,t), \mathbf{V}(d,t), T_{sd}(d,t)$ etc associated with a node d shown in Figure 3, is obtained with a volume averaged procedure in the Delaunay supercell Ω_d following,

$$X(d,t) = \sum_{D=1}^{cells} X(D,t)\Omega_D \Big/ \Omega_d \tag{15}$$

For steady U3DSMC simulations we obtain after reaching steady-state $m = 1, \mathrm{M}$ independent cell-based or nodal-based samples. The sample-averaged mean macroscopic property for a node (or cell) is denoted by $X_{sd(D)} \equiv n_{sd(D)}, \mathbf{V}_{sd(D)}, T_{sd(D)}$ etc and is given by

$$X_{sd(D)} = \sum_{m=1}^{\mathrm{M}} X_{sd(D)}^m \Big/ \mathrm{M} \tag{16}$$

Several flux properties, such as pressure, shear stress and heat flux ($\mathrm{W/m^2}$) to a solid surface, are determined from the perpendicular or parallel momentum and total energy exchange of the impinging particles. For example for heat flux,

$$q_s = \sum_{j} F_W \left[\left(E^*\right)_j - \left(E\right)_j \right] \Big/ A_s \Delta t \tag{17}$$

In the above, E^* is the reflected translational and internal energy of impinging particles on surface area A_s, and Δt is the duration of impingement sampling.

1.3 Validation of U3DSMC for Micro-scale Flows

The U3DSMC code was validated for micron-scale computations by comparisons with previous 2d DSMC results of Liou and Fang (2001)[15] and Le et al. (2007)[16] These simulations involved supersonic nitrogen flow incoming into a microchannel with height of 1.2 μm, length 6 μm and represent the smallest scales available in the literature for comparison. The domain used in the U3DSMC simulations is depicted in Figure 2. The incoming nitrogen $\mathrm{N_2}$ flow has $n_\infty = 1.75 \times 10^{25}\ \mathrm{m^{-3}}$, $T_\infty = 300\mathrm{K}$, $V_\infty = 1465.7$ m/s corresponding to $P_\infty = 72450\,\mathrm{Pa}$, $M_\infty = 4.15$, and $\lambda_\infty = 74.4$ nm, $Kn_\infty = 0.062$. Following [15, 16] the first $0.1L$ of the length of the computational domain is assumed to be specularly reflecting in order to generate uniform free-stream condition inside the microchannel. The supersonic incoming conditions are applied at the inlet of the computational domain. A vacuum outlet boundary condition is specified at the exit of the microchannel. Particles that leave the exit are removed from the domain and no particles are allowed to return into the domain. The upper and lower walls of the microchannel are isothermal at a constant temperature of 323 K and are assumed to be fully diffuse with perfect thermal accommodation. The side walls are simulated as specu-

lar so that they act as symmetry planes. In order to compare with the 2 D results, the depth D of the microchannel in our 3D simulations was varied and it was found that results are not sensitive for $D \geq \lambda_\infty$. A $D = 74.4$ nm was used in the simulations. The domain is discretized with 23032 Delaunay cells with 405 particles/cell upon loading and $\Delta\tau = 1 \times 10^{-13}$ sec. Macroscopic flow properties are sampled once steady state is reached. Twenty samples are used in obtaining the average after reaching the steady state time.

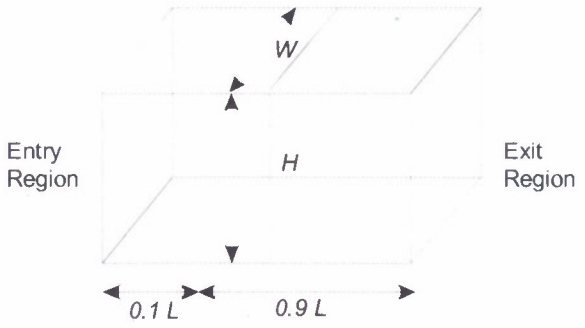

Figure 3. Geometry used in the U3DSMC simulation of a microchannel flow for comparison with 2D DSMC simulations of Liou and Fang [15] and Le et al. [16]

Figure 4 shows the centerline $y / H = 0.5$ translational temperature profile given in Eq. (11) obtained from the U3DSMC simulation. The difference between Liou and Fang, Le et al. and our 3d results is less than 7%. Figure 4b shows an excellent agreement between the velocity profiles obtained for $x / L = 0.5$. Figure 4c shows a good agreement with the heat flux at the wall. Differences in heat flux rates between the 3d and 2d simulations can be attributed to the sidewalls present in our 3d simulations as well as the sampling techniques used to obtain this surface fluxal property.

1.4 Statistical Error and Fluctuations in the U3DSMC Method

In a dilute gas there are inherent statistical fluctuations in macroscopic parameters such as number density, mean velocity, temperature, that are provided by theoretical estimates. In the case of a particle simulation such as the U3DSMC, these statistical fluctuations result to statistical errors due to the small number of particles used to represent the real number of particles in the domain, and the sampling associated with estimation of macroscopic variables. Such fluctuations and errors when compared to theoretical estimates, are functions of the particle weight (F_w), the volume of the Delaunay cells (Ω_D), the time-step ($\Delta\tau$) used, and the number of samples (M) used to obtain macroscopic properties. We followed Hadjiconstantinou et al. (2000)[17] and generalized their derivation for 3D unstructured grids used in U3DSMC considering a gas of species s particles.

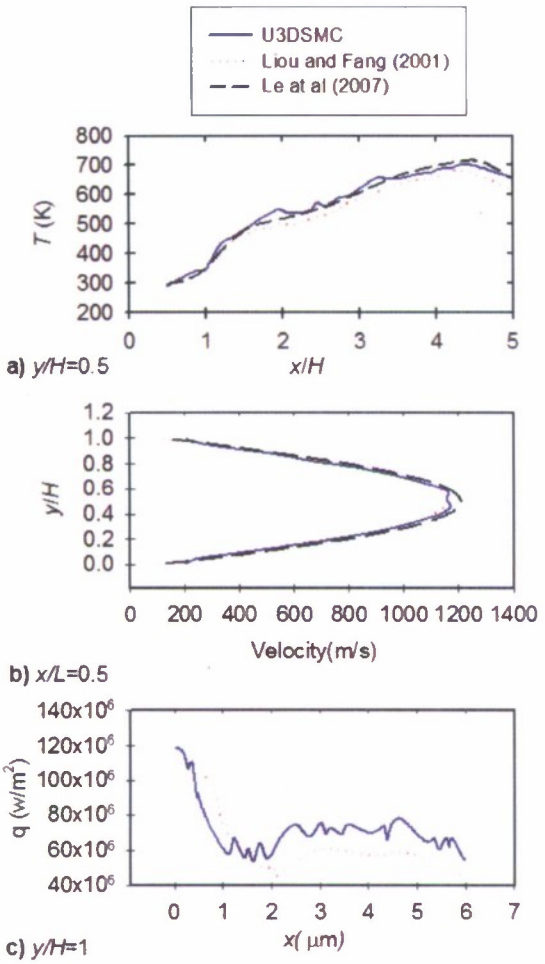

Figure 4. Temperature along centerline, mean velocity at *x/L*=0.5, and heat flux to the wall, in a micro-channel flow. Comparison between U3DSMC with 2D DSMC results of Liou and Fang [15] and Le *et al.*[16]

We considered the fluctuations associated with three important macroscopic fields, the number density (n), mean velocity (V) and translational temperature (T) obtained over $m = 1, \mathrm{M}$ samples as shown in eq. (16) The sample standard deviation for any cell-based variable at the *m*-th sample $X_D^m \equiv n_D^m, \mathbf{V}_D^m, T_D^m$ is defined as

$$\sigma(X_D^m) = \left[\frac{1}{\mathrm{M}-1}\sum_{m=1}^{\mathrm{M}}\left(X_D^m - X_D\right)^2\right]^{1/2} \tag{18}$$

and the standard deviation (uncertainty) of any sample-averaged mean variable $X_D \equiv n_D, \mathbf{V}_D, T_D$ obtained from eq. (16) is

$$\sigma(X_D) = \sigma(X_D^m)\Big/\sqrt{\mathrm{M}} \tag{19}$$

The fractional error of a sample-averaged mean variable, is defined as the standard deviation of the mean over the mean

$$E_{X_D} = \frac{\sigma(X_D)}{X_D} \tag{20}$$

The theoretical fractional error in the number density in a Delaunay cell is

$$E_n \equiv \frac{\sigma_n}{n_D} = \frac{\sigma_N}{N_D} = \frac{1}{\sqrt{\mathrm{M}N_D}} \frac{1}{Ac} \tag{21}$$

In the above equation the acoustic number is $Ac = a/a_t$, where a is the speed of sound, and $a_t = \sqrt{\gamma k T_o / m}$ is the speed of sound at a reference temperature. For dilute gases Ac=1. Similarly, the fractional error in the mean velocity component V_{xD} is

$$E_V \equiv \frac{\sigma(V_{xD})}{V_{xD}} = \frac{1}{\sqrt{\mathrm{M}N_D}} \frac{1}{AcM\sqrt{\gamma}} \tag{22}$$

where $\gamma = c_p / c_v$ is the ratio of specific heats and the Mach number is $M = V_{xD}/a$. The fractional error in temperature is

$$E_T \equiv \frac{\sigma(T_D)}{T_D} = \frac{\sqrt{\langle (\delta T)^2 \rangle}}{T_D \sqrt{\mathrm{M}}} = \frac{1}{\sqrt{\mathrm{M}N_D}} \sqrt{\frac{k_B}{C_v}} \tag{23}$$

where, C_v is the heat capacity at constant volume. The equations (21), (22), and (23) provide also the statistical error for sample-averaged nodal variables $X_d \equiv n_d, \mathbf{V}_d, T_d$ based on M instantaneous nodal samples, $X_d^m \equiv n_d^m, \mathbf{V}_d^m, T_d^m$. The same equations provide also the fractional error in the real gas if used with the real number of particles in the Delaunay or the super-Delaunay cell, $\mathrm{N}_{D(d)} = N_{D(d)} F_W$.

1.4.1 *Supersonic and Subsonic Nanoscale Flows*

In order to evaluate the statistical fractional errors in U3DSMC nanoscale simulations, we performed simulations for a flow of N_2 with $n_\infty = 2.69 \times 10^{25}$ m^{-3}, $T_\infty = 273$ K, $V_\infty = 3369.17$ m/s, $M_\infty = 10$ with $\lambda_\infty = 48.1$ nm, in a domain that requires the discretization of a characteristic length scale $L = 50$ nm. This set of conditions corresponds to one of the most restrictive for U3DSMC computation cases due to the smallest mean-free path involved. These U3DSMC simulations were realized in a rectangular domain of $(H \times W \times D)$ region with $H = W = 0.05$ μm and $D = 10$ μm. The simulations were run with $\Delta\tau = 1 \times 10^{-12}$s and steady state was achieved after 10^4 time steps by monitoring the mass flow rate at the exit. The domain was discretized with $G_D = 2446$ Delaunay

cells with an average volume $\langle \Omega_D \rangle = 9.9 \times 10^{-24} \mathrm{m}^3$, average edge-length $\langle l_D \rangle = 0.0438\ \mu\mathrm{m}$ and an average number of real particles per cell, $\mathrm{N}_D \simeq 266$. Two weights were used in the simulations, $F_W = 26$ with $N_D = 10$ computational particle per cell, and $F_W = 9$ with $N_D = 30$. The results from the U3DSMC simulations provided M = 460 Delaunay samples that were used to obtain sample-averaged n_D, V_D, T_D following eq. (16). The standard-deviation σ_X is evaluated from eq. (19), and subsequently eq. (20) provides the numerical error, designated as $E_X(\mathrm{U3DSMC})$. We also evaluated the fractional error using eq. (21), (22), (23) with U3DSMC parameters, and designate as $E_X(\mathrm{U3DSMC\ Analytical})$. Finally, we evaluated the error $E_X(\mathrm{Real\ Analytical})$ following equations (21), (22), (23) using the real number of particles in the sampling cell .

Figure 5 shows the fractional error as a function of the computational particles N_D and thus particle weight. The results show that U3DSMC simulations using particle weights as small as 9, have numerical fractional errors that compare very well with the analytical U3DSMC errors. It is therefore, desirable to use the theoretical formulas eq. (21), (22), (23) in estimating the fractional errors in a U3DSCM simulation instead of calculating the computationally expensive numerical fractional errors. The results from Figure 5 also show that the theoretical fractional errors in the real gas are within the same order of magnitude as the numerical errors. These results show that the no-time-counter (NTC) collision methodology implemented in U3DSCM is robust even with such small particle weights. If the particle weight becomes 1, then certain algorithmic steps in NTC could require modifications that are outside the scope of this work. Figure 6 illustrates the effect of Mach number on the fractional error E_V using the same number of samples as before. The fractional error for the subsonic case $M = 0.1$ is two order of magnitudes larger than the supersonic $M = 10$ a direct result of eq. (22). Our results are consistent with similar findings in structured DSMC computations found in Hadjiconstantinou et al. (2003)17.

1.4.2 *Subsonic Nanoflow*

A pressure driven subsonic flow of N_2 was also simulated using the U3DSMC. The geometry that is considered is a nanochannel of 500 nm height and 100 nm width 4 μm length. We assumed a mean flow with $n_\infty = 2.69 \times 10^{25}\ \mathrm{m}^{-3}$, $T_\infty = 273\ \mathrm{K}$ corresponding to atmospheric conditions with a $p_\infty = 101325$ Pa (1 atm) and $\lambda_\infty = 48.1$ nm. With P_{in}, and T_{in} specified, V_{in} was obtained from the inflow boundary condition method described in Sec. 1.2.4, and used for particle injection at the inlet boundary during the iteration.

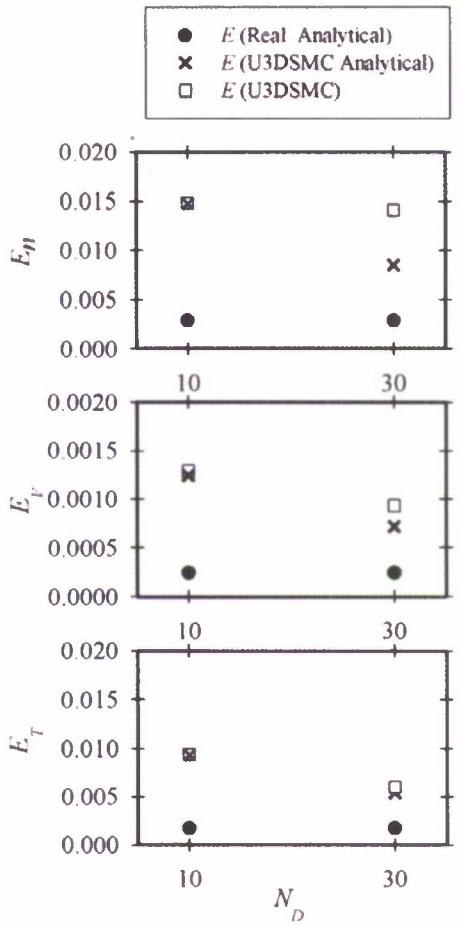

Figure 5. Statistical fractional errors in sample-averaged macroscopic density, velocity and temperature in a nanoscale flow. The U3DSMC errors are a function of the number of computational particles in a Delaunay cell. The real analytical error is based on the real number of particles in a Delaunay cell.

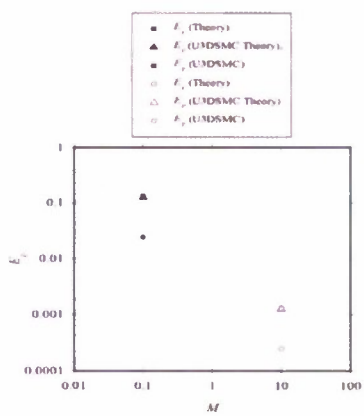

Figure 6. Statistical error in mean velocity for the uniform flow as a function of the Mach number.

Figure 7 shows the fractional error in the number density, mean axial velocity, and temperature as a function of the transverse direction (y). The U3DSMC errors are almost identical with the errors obtained from the theoretical expressions using the local values obtained from the U3DSMC and the real number of particles. The error in density and temperature shows no dependence on the transverse position. The error in mean velocity depends on the position. The minimum error occurs at the center of the channel where the maximum velocity is achieved

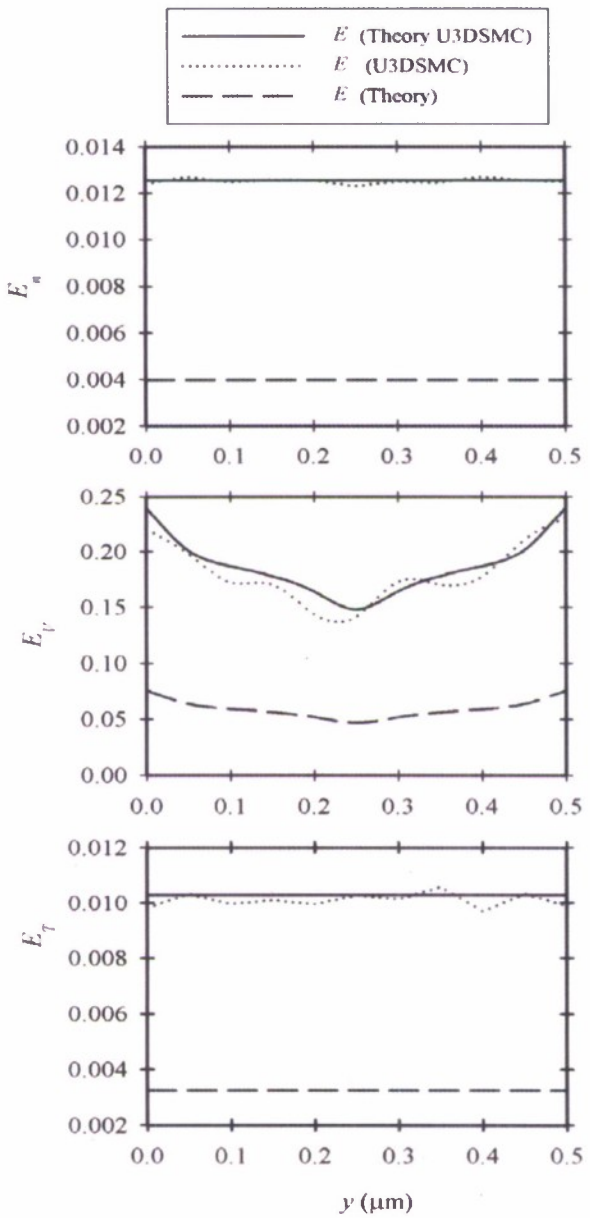

Figure 7. Statistical error in the U3DSMC simulation of a pressure driven nanoflow.

1.5 U3DSMC Computation of Nanoscale Flows

Gas flows in microscale channels have been studied extensively due to their relevance to micro-machined and MEMS devices or sensors. In the case of continuum and slip flow regimes characterized by the inlet Knudsen number based on the height H of the microchannel $Kn_\infty = \lambda_\infty / H$, analysis and simulations are usually carried out with Navier-Stokes type of solvers. In the case of transitional and free-molecular regimes ($Kn_\infty \geq 0.01$), analysis and simulations are carried out with Boltzmann solvers, most often based on the Direct Simulation Monte Carlo (DSMC) method. The DSMC has undergone various algorithmic improvements (Bird et al., 2009)[18] since its introduction and has become the primary method for simulating gaseous flows in microdomains.(Karniadakis et al., 2005[19]; Liou and Fang, 2006[20]. While there is a large number of investigations covering subsonic flows in microchannels, there is a smaller number covering supersonic microflows and very few investigations cover the sub-micron or nanoscale regime. The research performed under this grant provided a first insight on supersonic flows in nanoscale rectangular channels. The simulations performed with the U3DSMC code, covered the transitional to near-free molecular regimes. (Al-Khouz, 2009)[3].

Rarefied supersonic flows through channels and tubes has been studied analytically[21] and computationally using DSMC due to its importance in many technical applications.[22, 23, 24] For microchannels the 2d DSMC simulations so far have addressed the slip to transitional regimes for nitrogen and helium gases. [25, 26, 15, 27, 16] Microchannel heights considered in these investigations are in the range 0.1-2.4 microns with aspect ratios of 2.5-5 and Knudsen numbers in the range 0.0046 to 0.744 covering the slip and translational regimes. These DSMC investigations so far considered fully diffuse walls. In Mavriplis et al.(1997)[26] and Oh et al. (1997)[25] the wall temperature was specified to be equal to the free stream. In Liou and Fang (2001)[15], Le and Hassan, (2006)[27] and Le et al. (2007)[16] the wall temperature was set higher than the free stream for parts of the microchannels to investigate the heat transfer phenomena. These investigations have shown that a rarefied supersonic flow incoming into a macro- or microchannel with height H and length L is influenced by the free-stream Knudsen number Kn_∞, the free-stream ratio of mean speed over the most probable speed S_∞, the aspect ratio of the channel $\mathrm{AR} = L / H$, the wall temperature, the nature of wall reflection, and the type of molecules involved.

1.5.1 *Free stream, Boundary Conditions and Computational Parameters*

The supersonic flow into a rectangular nanochannel was investigated with the U3DSMC code for the geometry shown in Figure 8. The simulation domain featured a buffer region with length L_B, shown

in Figure 8, followed by the nanochannel with length, height and width L, H, W respectively. The flow is characterized by the Knudsen number

$$Kn = \frac{\lambda}{H} = \frac{1}{\sqrt{2}\pi d_{ref}^{\ 2} n \left(T_{ref}/T\right)^{\omega-1/2}} \frac{1}{H} \tag{24}$$

with $d_{ref} = 4.17 \times 10^{-10}$ m, $T_{ref} = 273$ K and $\omega = 0.74$.[8] The local speed-ratio is defined in eq. (5) and the local Mach number is given in terms of the specific heat ratio $\gamma = 1.4$, particle mass $m = 4.68 \times 10^{-26}$ kg, as

$$M = V \Big/ \sqrt{\frac{\gamma k T}{m}} \tag{25}$$

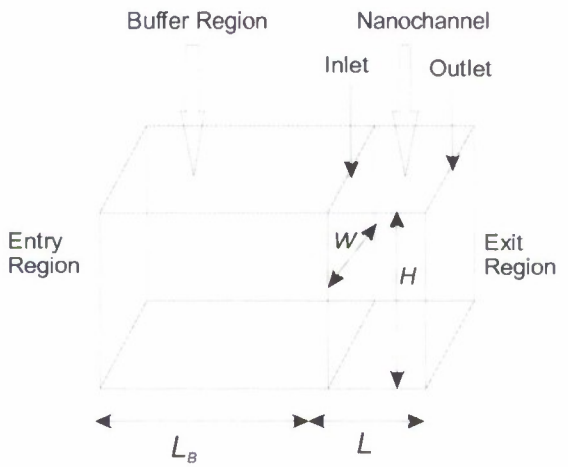

Figure 8. The computational domain used in the U3DSMC simulations of nanochannel flows (dimensions not to scale).

Rectangular nanochannels with $H = W = 100 - 1000$ nm, AR=1, 10, 100 are considered in the simulations with input parameters shown in Table 1. The incoming nitrogen N_2 flow has $n_\infty = 2.69 \times 10^{24}\,\mathrm{m}^{-3}$, $T_\infty = 273$K, corresponding to $P_\infty = 0.1$ atm (10.132 kPa) and $\lambda_\infty = 481$ nm. Cases 1-9 have $V_\infty = 2013$ m/s, $S_\infty = 5$ and $M_\infty = 5.97$. Case 10 has $V_\infty = 805.2$ m/s, $S_\infty = 2$, $M_\infty = 2.39$. Case 11 has $V_\infty = 4026.8$ m/s, $S_\infty = 10$ and $M_\infty = 11.95$. In the simulations we consider the rotational but neglect the vibrational degrees of freedom of the nitrogen.

In order to allow for the undisturbed free stream conditions to be realized far from the nanochannel inlet we included a buffer region of length L_B ahead of the nanochannel inlet. Molecules were injected through the boundaries of the buffer region based on eq. (6) with specified $n_\infty, T_\infty, V_\infty$. The

sides of the buffer region were modeled as a free stream. Particles that moved upstream and reachEd the surfaces of he buffer region were removed from the computational domain.

Table 1. Physical and computational parameters for U3DSMC simulations of nitrogen subatmospheric nanochannel flows.

Case	H (nm)	L/H	S_∞	M_∞	P_b (kPa)	Kn_∞	L_B (nm)	G_D	$\langle l_D \rangle$(nm) [$\sigma(l_D)$]	F_W	$\langle N_D \rangle$ [$\sigma(N_D)$]
1	100	1	5	5.97	0	4.81	1000	132	85.8 [8.74]	20	11.21 [4.44]
2	100	10	5	5.97	0	4.81	1000	252	85.2 [7.2]	20	10.67 [3.78]
3	100	100	5	5.97	0	4.81	1000	504	122 [17.8]	20	29.36 [10.96)]
4	500	1	5	5.97	0	0.962	1000	1544	118 [12.1]	20	32.67 [11.93]
4a	500	1	5	5.97	120	0.962	100	1544	118 [12.1]	20	32.67 [11.93]
4b	500	1	5	5.97	200	0.962	100	1544	118 [12.1]	20	32.67 [11.93]
5	500	10	5	5.97	0	0.962	1000	5836	129 [11.4]	20	34.57 [11.03]
5a	500	10	5	5.97	40	0.962	1000	5836	129 [11.4]	20	34.57 [11.03]
5b	500	10	5	5.97	100	0.962	1000	5836	129 [11.4]	20	34.57 [11.03]
6	500	100	5	5.97	0	0.962	1000	48576	135 [9.26]	20	35.30
7	1000	1	5	5.97	0	0.481	1000	8276	125 [10.4]	20	32.5 [11.00]
8	1000	10	5	5.97	0	0.481	1000	45194	128 [10.1]	20	72.1 [10.5]
9	1000	100	5	5.97	0	0.481	3000	425576	400 [34.8]	100	199.51 [74.38]
10	500	10	2	2.39	0	0.962	1000	5836	129 [11.4]	20	34.57 [11.03]
11	500	10	10	11.95	0	0.962	1000	5836	129 [11.4]	20	34.57 [11.03]

The outlet of the nanochannel was placed at the exit boundary of the computational domain as shown in Figure 8. A vacuum boundary condition was set for Cases 1-11, where the back pressure is specified as $P_b = 0$ at the exit region. Any particle reaching the exit plane was removed from the domain and no particles were allowed to enter the computational domain through the exit plane. For Cases 4a, 4b and 5a, 5b a finite back pressure P_b was specified at the exit. The upper and lower walls, as well as the side walls of the nanochannel, were modeled as fully diffuse and the temperature of the

wall equals that of the free stream distribution. The simulation domain was loaded initially with a uniform drifting gas following eq. (6) based on the free stream conditions in Table 1.

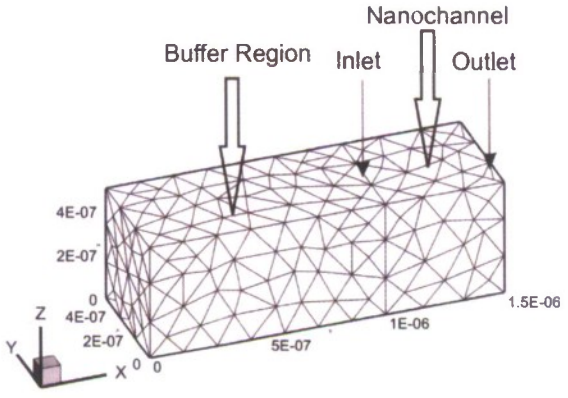

Figure 9. Typical grid used in U3DSMC simulations (Case 4) showing the surface elements of the Delaunay tethrahedra.

Figure 9 displays the boundary faces of the Delaunay cells of a typical mesh used in the simulations. The interior is discretized with Delaunay tethrahedra cells with edge-lengths that are smaller than λ_∞. The mean of the Delaunay edge lengths $\langle l_D \rangle$ in Table 1 show that they are about one fourth of the corresponding $\lambda_\infty = 481$ nm. The total number of Delaunay cells in the domain G_D, the average number of simulated particles in each cell $\langle N_D \rangle$ and its standard deviation $\sigma(N_D)$ are provided in Table 1. These parameters show that the Delaunay cells are populated at initialization with at least 10 computational particles.

The collision time under free stream conditions is on the order of 10^{-9} s and can become on the order of 10^{-11} s for higher densities and temperatures encountered in the nanochannels considered in these simulations. From the parameters in Table 1 the most restrictive convective time scale $\langle l_D \rangle / V_\infty$ is on the order of 10^{-11} sec. The simulations were run with a time step $\Delta\tau = 10^{-12}$ s to ensure decoupling of particle motion with collisions, and ensure that computational particles do not cross a cell prior to a collision. The steady state time was determined from the mass flow rate obtained at the outlet of the nanochannel, as shown in Figure 10. After reaching the steady state time of 0.2 μsec, 100 nodal samples obtained following the volume average procedure of eq. (15), corresponding to more than 2,000 Delaunay samples, were averaged to produce the steady-state flow properties following eq. (16). The 10^{-10} seconds (100 time steps) allowed between two successive nodal samples combined with the large number of Delaunay samples used in obtaining each nodal sample, provides some assurance for the statistical independence of the samples.

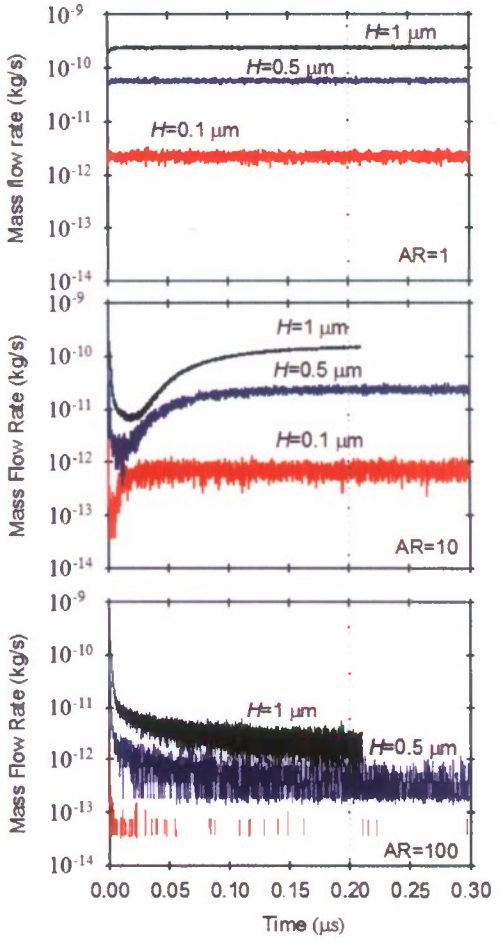

Figure 10. Mass flow rate from U3DSMC simulations at the outlet of a rectangular nanochannel with $P_\infty = 0.1$ atm , aspect ratio AR, and height *H* (Case 1-9). The dotted line shows the steady-state time used to obtained samples for the evaluation of macroscopic variables.

1.5.2 *Grid Sensitivity Analysis*

The cell size is an important parameter in a DSMC simulation and for microflows it has been examined extensively for 2D uniform grids.[28, 17] For the unstructured 3D simulations in this work the grid was generated using nearly equally sized tetrahedra. While the distribution of edge-lengths is nearly uniform, the mean $\langle l_D \rangle$ is the proper representative cell scale. The grid sensitivity analysis studied the effect of increasing the cell size using as baseline parameters presented in Table 1 and comparing macroscopic flow parameters such as density, flow velocity and translational temperature.

Table 2. U3DSMC simulation parameters used in the grid sensitivity study.

Case	$\langle l_D \rangle$ (nm) [λ]	$\sigma(l_D)$ (nm)	$\langle N_D \rangle$	$\sigma(N_D)$
2	85.2 [1/5.6]	8.74	11.21	4.44
GS-2	136 [1/3.4]	11.7	35.87	13.73
4	129 [1/3.4]	11.4	34.57	11.03
GS-4	205 [1/2.3]	17	57.5	11.2

Results for the two most restrictive Cases 2 and 4, i.e. nanochannels with the small inlets and aspect ratios, are discussed bellow. Input parameters of Case 2 and Case 4 are used in simulations GS-2 and GS-4 with nearly doubling the edge-length l_D while keeping the particle weight constant at $F_W = 20$. The resulting $\langle l_D \rangle$ and $\langle N_D \rangle$ are shown in Table 2.

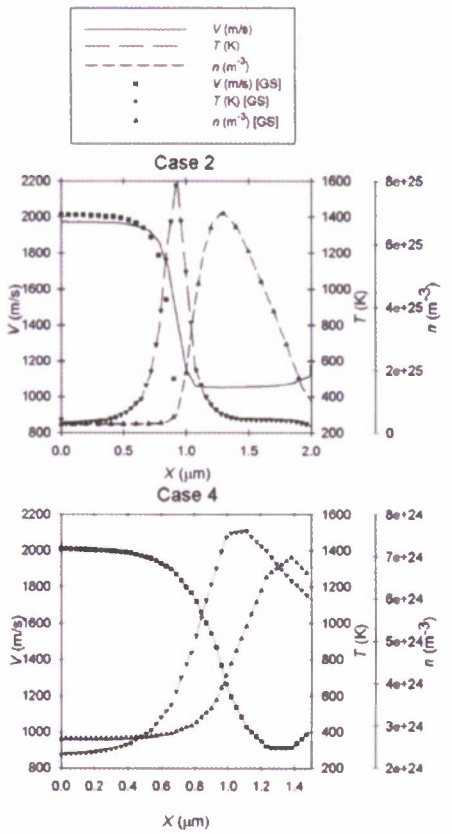

Figure 11. Centerline values of n, V_x, T. Top: Case 2 (lines) and Case GS-2 (symbols) Bottom: Case 4 (lines), Case GS-4 (symbols).

Centerline values for the number density, translational temperature, and mean velocity are shown in Figure 11. Case 2 and Case GS-2 represent a near free-molecular flow with $Kn_\infty = 4.81$,

$H = 0.1\,\mu\text{m}$ and AR=10. Figure 11 shows that doubling the size of the edge-length, while keeping it smaller than λ_∞, has no effect on centerline flow properties. Case 4 and Case GS-4 correspond to a transitional flow with $Kn_\infty = 0.481$, $H = 0.5\,\mu\text{m}$ and AR=1. A comparison between Case 4 and GS-4 flow properties in Figure 11 shows that the doubling of the edge-length has no effect on the centerline flow properties. These results obtained for the most restrictive cases, provide evidence that the choice of computational parameters used in the nanoscale simulations, provide sufficient numerical resolution.

1.5.3 *Summary of Simulation Results*

1.5.3.1 *Effects of Nanochannel Inlet Size and Aspect Ratio*

These effects were examined with Case 1 to Case 9 simulations shown in Table 1. The inlet height establishes the free stream Knudsen number and characterizes the rarefaction effects. The aspect ratio, AR, establishes the flow development due to particle-wall interactions.

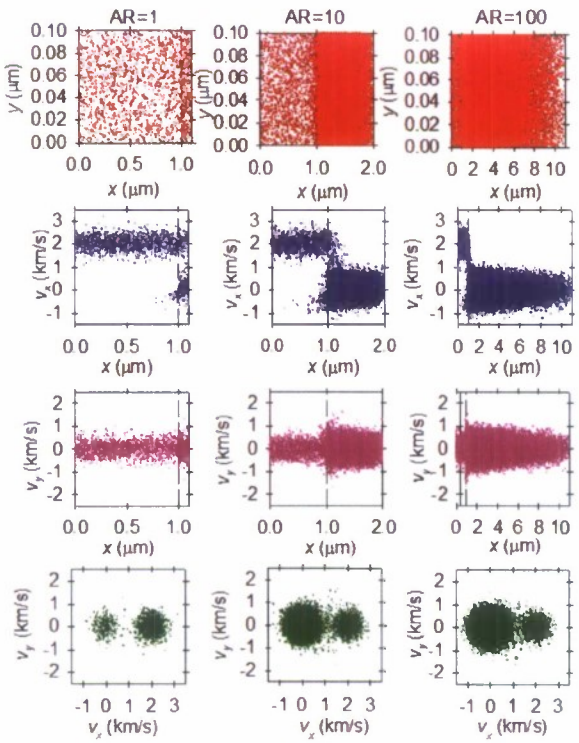

Figure 12. Effects of the aspect ratio AR=*H/L* on phase-space (x, y), (x, v_x),(x, v_y), (v_x, v_y) obtained from the U3DSMC simulation of a supersonic flow into an *H*=0.1 μm nanochannel (Case 1, 2 and 3). The $P_\infty = 0.1$ atm free stream is to the left of the 1 μm buffer region with the nanochannel inlet indicated by the dotted line.

The phase space for Cases 1, 2 and 3 is presented in Figure 12. These cases simulate the smallest nanochannels with $H = 0.1\,\mu\text{m}$ and correspond to the near free-molecular flow with a $Kn_\infty = 4.81$. The (x, y) phase plot shows the number density to increase inside the AR=1 nanochannel. The AR=10, and AR=100 nanonchannels show an increase in the number density followed by a decrease at the end of the nanochannel. The (x, v_x) phase plot shows the high-speed free-stream population to permeate the entire length of the AR=1 nanochannel. The (x, v_x) plot shows that inside the AR=1 nanochannel a low-speed population develops as a result of collisions of particles with the walls. In addition, a small population of upstreaming particles exit from the inlet after colliding with the walls or other particles in the density enhancement region. The (x, v_x) plot for the AR=10 and AR=100 cases shows that the high-speed component does not permeate the entire length of the nanochannel. Instead, the nanochannel is populated with near zero-drift particles, due to diffuse reflections off the walls. The (x, v_x) phase space for AR=10 and AR=100 shows that the spread of the v_x component is reduced towards the exit. Both phase plots exhibit the upstreaming particles. The (x, v_y) phase plots in Figure 12 show that the y-component of the velocity increases inside the nanochannel as a result of the collisions in the density enhancement region. As the AR increases from 1 to100, the velocity spread decreases with increasing length, due to diffuse reflections off the walls. The (v_x, v_y) phase plots in Figure 12 corroborate the previous results. The AR=1 nanochannel shows the appearance of a symmetric, free-streaming population and a secondary, symmetric, zero-drift population that arise due to collisions with the wall. This zero-drift population becomes the dominant feature of the flow as the AR increases. It is also noticeable that the spread, that is the temperature of the low-drift population, is larger than the free-stream value as a result of collisions inside the nanochannel. The symmetry of the low-speed population is indicative of gas-wall equilibration phenomena inside the nanochannel.

In Figure 13 we plot the sample-averaged, macroscopic fluid properties along the centerline of the nanochannel and the buffer region. They include the number density from eq. (7), the average velocity V_x from eq. (8), and the translational temperature T from eq, (11). These macroscopic variables are sampled in Delaunay cells, shown in Figure 2, that occupy a considerable fraction of the nanochannel at a given downstream position. With a few sampling cells spanning the width of the nanochannel it is not feasible to obtain a meaningful spatial resolution and construct contour plots. The number density shows the formation of the density enhancement that becomes stronger with increasing AR for all Knudsen numbers considered. The density decreases inside the nanochannel and the trend is more pronounced with the larger AR cases.

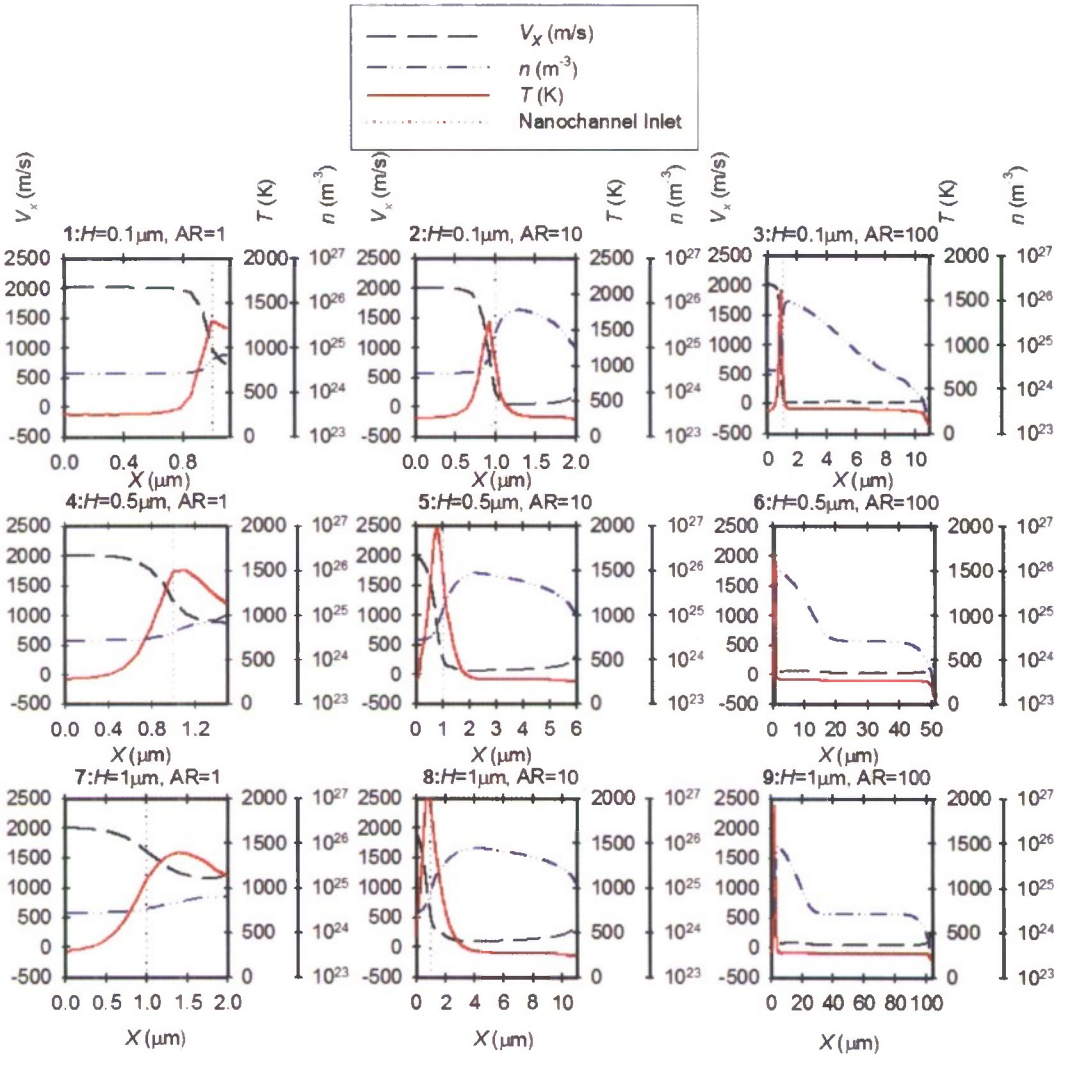

Figure 13. Centerline, sample-averaged, macroscopic flow properties (V_x,T, n) in a nanochannel obtained from U3DSMC simulations (Cases 1-9). The $P_\infty = 0.1$ atm free stream is to the left of the 1 μm buffer region with the nanochannel inlet indicated by the dotted line.

The density enhancement is explained physically with the phase-space plots discussed earlier. The average velocity decreases near the inlet of the nanochannel for all cases considered. The temperature shows an enhancement in the inlet region and it is associated with the presence of the high-speed and low-speed particle populations shown in the phase plots of Figure 12. The temperature after the inlet region shows a sharp decrease and remains almost constant for the AR=10 and AR=100 nanochannels indicating equilibrium with the wall temperature. As Table 1 shows in cells with $n_D \simeq n_\infty$ the num-

ber of computational particles is $\langle N_D \rangle \simeq 10 - 40$ and in cells with $n_D > n_\infty$ the value of $\langle N_D \rangle$ can be even larger. The numerical fractional errors in the sample-averaged density, velocity and temperature are expected to be below the range given in Figure 5.

For all cases considered the density maximum is located near the inlet but inside the nanochannel. The temperature maximum is located before or at the inlet of the nanochannel. This behavior where density and temperature enhancement do not coincide has been observed in rarefied high-speed flows into macroscale tubes Gatsonis *et al.* (1997)24 as well microchannels (Oh *et al.*, 1997;[25] Liou and Fang, 2001;[15] Le and Hassan, 2007.[27]) The nanochannel acts a solid body to the incoming flow and reflected particles from the wall generate this perturbation region which is similar to a diffuse shock formed in front of a solid body in a high-speed rarefied gas flow (Wilmoth et al.,1992) [29].

In Figure 14 the centerline pressure from eq. (12) and Mach number are plotted for Cases 1-9. The AR=1 nanochannels show that the Mach number is supersonic at the inlet and remains supersonic for the three Knudsen numbers considered. The centerline pressure increases from its free stream value and decreases slightly towards the outlet. The nanochannels with AR=10 and AR=100 result in a subsonic inlet Mach number and a sharp increase in pressure near the inlet. The Mach number, subsequently, increases and reaches the sonic point at the outlet for all cases considered. For the supersonic inlet (Case 1, 4 and 7) in the AR=1 nanochannels, the Mach number remains supersonic at the outlet. For cases where the inlet Mach number becomes subsonic the flow becomes sonic at the exit. The pressure in Figure 14 shows a sharp increase in the density enhancement region near the inlet, followed by a decrease towards the end of the channel. Figure 13 and Figure 14 show the 1-μm buffer using the same *X*-axis size for simulation domains ranging from 1.1 μm (Case 1) to 101 μm (Case 9). Therefore, for some of the AR=10 and AR=100 cases the free stream conditions cannot be depicted clearly. While there are variations in the flow parameters in the buffer region, the free stream conditions are sustained at the entry of the 1-μm buffer region for all cases considered.

1.5.3.2 *The Effects of Free Stream Speed Ratio and Back Pressure*

The free stream speed ratio can have profound effects on the flow characteristics inside a nanochannel. Simulations for $H = 0.5\mu$ and AR=10 nanochannels were performed with free stream speed ratios of $S_\infty = 2$ (Case 10) , $S_\infty = 5$ (Case 5) and $S_\infty = 10$ (Case 11). The effects of backpressure were examined in simulations Case 4, 4a, 4b, 5, 5a, 5b. These simulations were performed with $H = 0.5\mu$ and AR=1 and AR=10 nanochannels with free stream speed ratio of $S_\infty = 5$ and $P_\infty = 10.13\,\text{kPa}$. Discussion of the results can be found in Al-Khouz (2009).[3]

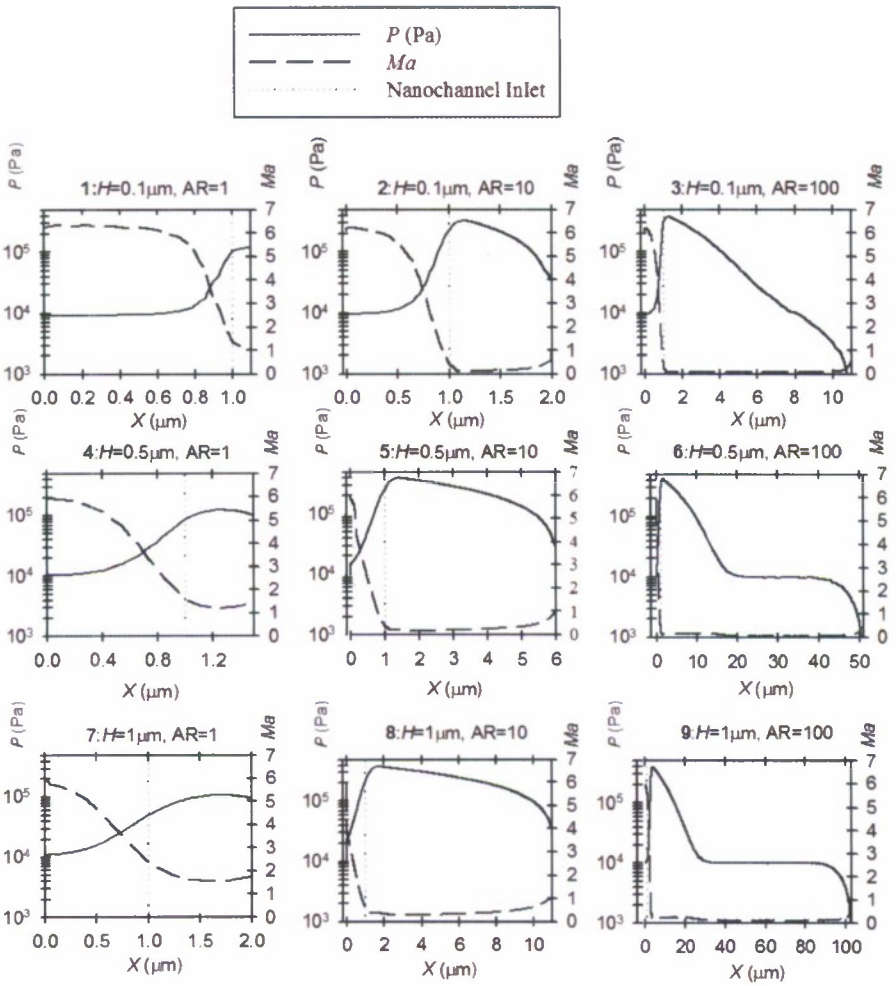

Figure 14. Centerline sample-averaged Mach number and pressure in a nanochannel obtained from U3DSMC simulations (Cases 1-9). The $P_\infty = 101{,}320$ Pa, $M_\infty = 5.97$ free stream is to the left of the 1 μm buffer region with the nanochannel inlet indicated by the dotted line.

1.5.4 *Validation of U3DMC at the Nanoscale*

The heat flux to the wall obtained from U3DSMC through eq. (17) is plotted in Figure 15. With the exception of the AR=1 nanochannels the heat loss is largest in the inlet region. A comparison between the numerical and theoretical values of heat loss can be obtained for Cases 1, 2, 3 that correspond to near-free molecular flows at $Kn_\infty = 4.51$. The free molecular, total translational and internal energy flux (or heat transfer rate) from a free stream with ρ, T, S to a flat plate with surface temperature T_r aligned with the flow is,

$$q_{th} = -nm\left(\frac{2kT}{m}\right)^{3/2}\frac{(1-\varepsilon)}{4\pi^{1/2}} \left\{\left[S^2 + \frac{\gamma}{\gamma-1} - \left\{\frac{1}{2}\frac{\gamma+1}{\gamma-1}\right\}\frac{T_r}{T}\right]\left[\exp\left(-S^2\right) + \pi^{1/2}S\left\{1+erf\left(S\right)\right\}\right] - \frac{1}{2}\exp\left(-S^2\right)\right\} \tag{26}$$

where ε is the fraction of molecules that is reflected specularly (Bird, 2000)[9]. Substituting in eq. (26) values for ρ, T, S from the U3DSCM results sampled at the inlet of the nanochannel we obtain theoretical values of heat flux. For Case 1, $q_{th} = -52.4\times10^6$ W/m^2 with the numerical $q = -31.3\times10^6$ W/m^2. For Case 2, $q_{th} = -93.7\times10^6$ W/m^2 and $q = -62.5\times10^6$ W/m^2. For Case 3, $q_{th} = -42.5\times10^6$ and $q = -19.8\times10^6$ W/m^2. The numerical values are, therefore, within the order of magnitude of the theoretical estimates of heat loss.

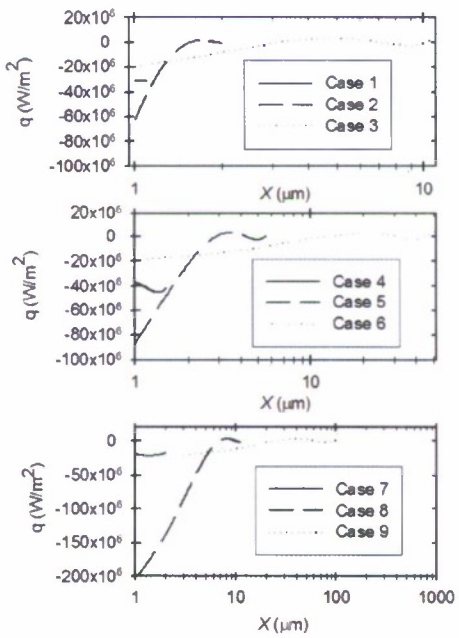

Figure 15. Heat flux to the wall obtained from the U3DSMC simulation of a supersonic flow into a nanochannel. The free stream is at *X*=0 μm and the nanochannel inlet at *X*=1 μm (Case 1-9).

The outgoing mass flow rate at the outlet from U3DSMC was also compared with estimates obtained using the semi-analytical theory developed for the free-molecular regime by Hughes and de Leeuw (1965)[21]. For a cylindrical tube with aspect ratio $D = d / L$, a drifting Maxwellian with a speed ratio at zero angle of attack with the tube axis, will have a flux of particles exiting at the outlet into a background of specified pressure given by

$$N(S_\infty, D, 0) = \frac{n_\infty C_{m\infty}}{2\sqrt{\pi}}\pi r^2 \int_0^{\pi/2} K(\phi, D)F(\phi, S_\infty, 0)d\phi \tag{27}$$

In the above, $C_{m\infty}$ is the most probable speed. The quantity $K(\phi, D)$ is the ratio between the number flux of molecules exiting at the outlet of the tube, and the number flux of particles that enter the tube due to a beamlet with an angle ϕ with the tube axis. Hughes and de Leeuw evaluate $K(\phi, D)$ using the Clausing's probability function for particle transmission after wall reflections. The flux term in eq. (27) that strikes a surface perpendicular to the tube axis at an angle between ϕ and $d\phi$, is,

$$F(\phi, S, 0) = \sin\phi\cos\phi[(1 + S^2\cos^2\phi)\exp(-S^2) + \pi^{1/2}S\cos\phi\exp(-S^2\sin^2\phi)(\tfrac{3}{2} + S^2\cos^2\phi)(1 + erfS\cos\phi)] \quad (28)$$

The expressions in eq. (27) have been integrated numerically and evaluated using input parameters from the simulations for Case 1-9. Comparisons are shown in Figure 16. For AR=1 and AR=10, the U3DSMC predictions are very close to the theoretical. For the long AR=100 nanochannels, the theoretical predictions are larger than the U3DSMC. The theory does not account for the external flow effects nor the internal structure of the flow field as evident in the U3DSCM results discussed earlier. In the case of short tubes, wall collisions are not sufficient to modify the free-stream and the theoretical results provide the outgoing flux.

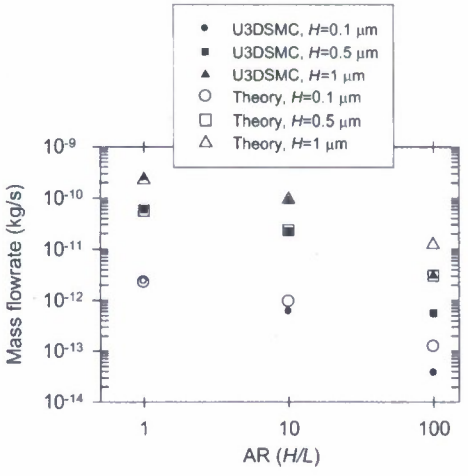

Figure 16. Outgoing mass flow rate at the outlet of a nanochannel for various aspect ratios. Comparison between U3DSMC simulations (Case 1-9) and numerical results obtained from the Hughes and de Leeuw [21] theory.

1.6 U3DSMC Simulation of Atmospheric-Pressure Supersonic Flows Into Nanochannels

We performed simulations of supersonic atmospheric flows into nanochannels using the U3DSMC method. Figure 8 shows the simulation domain as well as the parameters used to define the nanochannel and the buffer region geometries. The incoming free stream of nitrogen N_2 has $n_\infty = 2.69\times10^{25}\,\mathrm{m}^{-3}$, $T_\infty = 273\mathrm{K}$, corresponding to $P_\infty = 1\,\mathrm{atm}$ and $\lambda_\infty = 48.1$ nm. The free stream velocity V_∞ was varied in the simulations so that the speed ratio spans the range of the super-

sonic ($S_\infty = 2$) to hypersonic ($S_\infty = 10$) flow regimes. The variation of the inlet height results in Kn_∞ that range from 0.0962 to 0.481 covering the slip to transitional regimes. The parameters considered in these simulations are shown in Table 3. The simulations considered vacuum back pressure.

Table 3. Physical and computational parameters for U3DSMC simulations of atmospheric-pressure nitrogen flows into a nanochannel.

Case	H (nm)	L/H	S_∞	M_∞	P_b (kPa)	Kn_∞	L_B (nm)	G_D	$\langle l_D \rangle$ (nm) [$\sigma(l_D)$]	F_N	$\langle N_D \rangle$ [$\sigma(N_D)$]
1	100	1	5	5.97	0	0.481	1000	1578	8.62 [0.793]	12	13.47 [3.21]
2	100	10	5	5.97	0	0.481	1000	2793	8.45 [0.775]	12	14.34 [3.11]
3	500	1	5	5.97	0	0.0962	1000	57407	11.29 [1.21]	12	14.21 [3.07]
4	500	10	5	5.97	0	0.0962	1000	57879	18.08 [2.15]	30	22.8 [5.77]
5	100	10	2	2.39	0	0.0962	1000	2793	8.45 [0.775]	12	14.34 [3.11]
6	100	10	10	11.95	0	0.0962	1000	2793	8.45 [0.775]	12	14.34 [3.11]

The phase space plots for Case 1 and 2 are presented in Figure 17. These cases simulate the narrowest nanochannels with $H = 0.1\,\mu\text{m}$ and correspond to the transitional flow with a $Kn_\infty = 0.481$. The (x, y) phase plot shows that there is an enhancement in the number density inside the AR=1 nanochannel. The long AR=10 nanonchannel shows an increase in the number density followed by a decrease at the end of the nanochannel. The (x, v_x) phase plot shows the high-speed free-stream population to permeate the entire length of the AR=1 nanochannel. The (x, v_x) plot shows a low-speed population of particles that develops inside the AR=1 nanochannel as a result of collisions of particles with the walls. In addition, a small population of up streaming particles exit the inlet after colliding with the walls or other particles in the density enhancement region. The (x, v_x) plot for the AR=10 case show that the high-speed component does not permeate the entire length of the nanochannel. Instead, the nanochannel is populated with a near zero-drift particles due to diffuse reflections of the walls. The (x, v_x) phase space shows that the spread of the v_x component is reduced towards the exit. The (x, v_y) phase plots show that the y-component of the velocity increases inside the nanochannel as a result of the collisions in the density enhancement region. As the AR increases the velocity spread decreases with increasing length, due to diffuse reflections of the walls. The (v_x, v_y) phase plots cor-

roborates the analysis of the space-velocity phase plots. The AR=1 nanochannel show the appearance of a symmetric free-streaming population and a secondary, symmetric, zero-drift population that arise due to collisions with the wall. This zero-drift population becomes the dominant feature of the flow as the AR increases. It is also noticeable that the spread in v_y (which is an indication of the temperature) for the low-drift population is larger than the free-stream value as a result of collisions inside the nanochannel. The symmetry of the low-speed population is indicative of gas-wall equilibration phenomena inside the nanochannel. The complete set of results and discussion is presented in Al-Khouz (2009).[3]

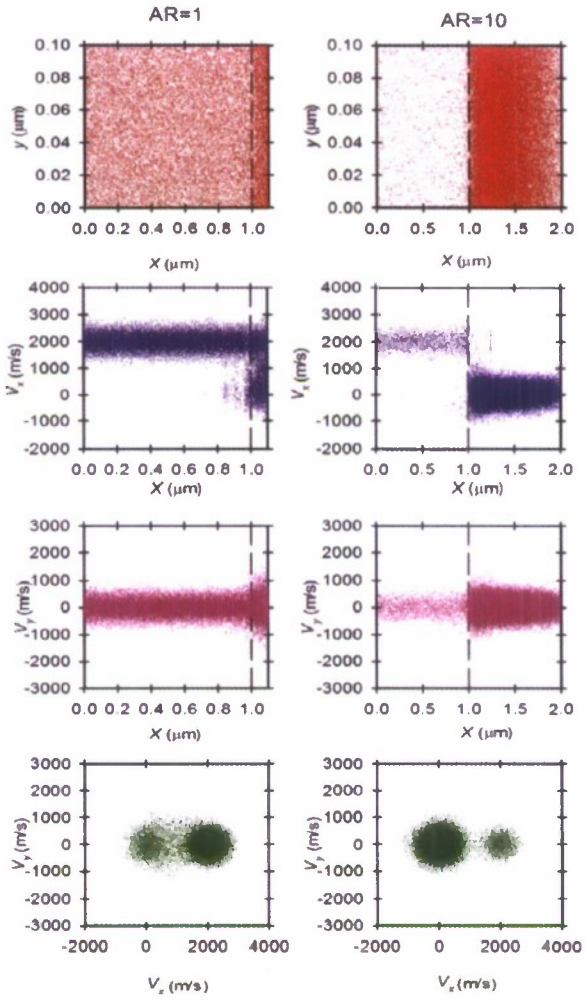

Figure 17. Effects of AR for *H*=0.1 μm nanochannels. Phase plots (x,y), (x,v_x), (x,v_y) and (v_x,v_y) for Case 1, 2.

1.7 Conclusions

The U3DSMC simulations in this work, featured a small number of real particles in the computational domain, small particle weights, and few computational cells across the width of the nanochan-

nel. The U3DSMC results showed that the supersonic nanoflows considered exhibit characteristics that are similar to previous micron- and macroscale flows covering similar Knudsen number regimes, and have physical characteristics that are found in continuous compressible, viscous channel flows with friction and heat loss. The microscopic analysis adopted in our work used the phase-space distributions and provided the kinetic-based explanation of the obtained macroscopic flow variables. Overall, our work extended the applicability of the U3DSMC method to rarefied supersonic nanoflows.

2 SMOOTHED DISSIPATIVE PARTICLE DYNAMICS

We review below the second major approach undertaken during this research involving particle simulation of fluid flows at the mesoscale. The Smooth Dissipative Particle Dynamics (SDPD) method developed by Espanol and Revenga, (2003)[30] is a Lagrangian, mesh-free, particle model that can be applied from microscale to nanoscale flow domain, as shown in Figure 18. SDPD can be derived as a top-down approach from SPH with the introduction of a fluctuation term. As a bottom-up approach, SDPD it is a thermodynamically consistent version of the original DPD, due to the introduction of the energy equation in the model.

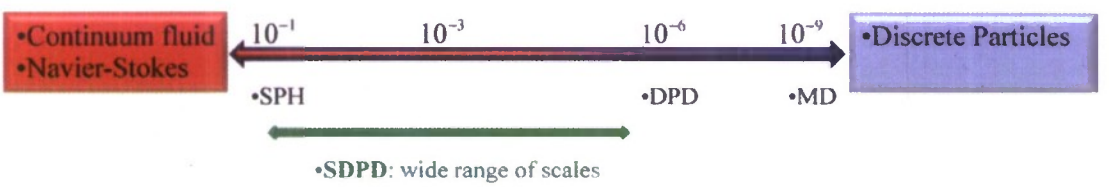

Figure 18. Length scales and computational approaches.

In SDPD the fluid particle with position $\mathbf{r}_i$ and velocity $\mathbf{v}_i$ has a volume defined as

$$\frac{1}{V_i} = d_i = \sum_{j=1}^{N} W(r_{ij}, h) \text{ with } r_{ij} = |\mathbf{r}_i - \mathbf{r}_j| \tag{29}$$

The supporting function is similar to the one found in SPH.[31] One choice based on the interaction length h is

$$W(r_{ij}, h) = \frac{105}{16\pi h^3}\left(1 + 3\frac{r_{ij}}{h}\right)\left(1 - \frac{r_{ij}}{h}\right)^3 \tag{30}$$

The density of the i-th SDPD particle is

$$\rho_i = m_i d_i = m_i \sum_{j=1}^{N} W(r_{ij}, h) \tag{31}$$

The mass

$$m_i = \frac{M_{TOT}}{N_{part}} \tag{32}$$

The SDPD particle position is

$$\mathrm{d}\mathbf{r}_i = \mathbf{v}_i dt \tag{33}$$

The SDPD momentum is given by

$$m_i \mathrm{d}\mathbf{v}_i = \sum_j \left[\frac{P_i}{d_i^2} + \frac{P_j}{d_j^2}\right] F_{ij}\mathbf{r}_{ij}\mathrm{d}t - \left\{\sum_j (1-d_{ij})a_{ij}\mathbf{v}_{ij}\mathrm{d}t + \sum_j (1-\chi_{ij})\left(\frac{a_{ij}}{3}+b_{ij}\right)\hat{\mathbf{e}}_{ij}\hat{\mathbf{e}}_{ij}\cdot\mathbf{v}_{ij}\mathrm{d}t\right\} + m\mathrm{d}\tilde{\mathbf{v}}_i \tag{34}$$

The first term in the momentum equation provides the conservative force. The pressure of an SDPD particle is derived from the equation of state

$$P_i = -\frac{\partial E^{state}}{\partial V_i} \tag{35}$$

The second group of terms in momentum, provides the dissipative force with a rotational and central component. The third term provides the random force

$$m\mathrm{d}\tilde{\mathbf{v}}_i = \sum_j \left(A_{ij}\overline{\mathrm{d}\mathbf{W}}_{ij}^S + B_{ij}\frac{\mathbf{1}}{3}tr[\mathrm{d}\mathbf{W}_{ij}]\right)\cdot\mathbf{e}_{ij} \tag{36}$$

The $d\mathbf{W}_{ij}$ is a matrix of independent increments of the Wiener process. Dissipative and random forces are related in SDPT through the temperature terms.

The entropy equation for the i-the SDPD particle is

$$\begin{aligned} T_i \mathrm{d}S_i = {} & \frac{1}{2}\sum_j \left(1-\chi_{ij}-\frac{T_j}{T_i+T_j}\frac{k_B}{C_i}\right)\left[a_{ij}v_{ij}^2 + \left(\frac{a_{ij}}{3}+b_{ij}\right)(\mathbf{e}_{ij}\cdot\mathbf{v}_{ij})^2\right]\mathrm{d}t \\ & - \frac{2k_B}{m}\sum_{j\neq i}\frac{T_iT_j}{T_i+T_j}\left(\frac{10}{3}a_{ij}+b_{ij}\right)\mathrm{d}t - \sum_j c_{ij}T_{ij}\mathrm{d}t - \frac{k_B}{C_i}\sum_{j\neq i}c_{ij}T_j\mathrm{d}t + T_i\mathrm{d}\tilde{S}_i \end{aligned} \tag{37}$$

The fluctuating term is

$$T_i\mathrm{d}\tilde{S}_i = -\frac{1}{2}\sum_j \left(A_{ij}\overline{\mathrm{d}\mathbf{W}}_{ij}^S + B_{ij}\frac{\mathbf{1}}{3}tr[\mathrm{d}\mathbf{W}_{ij}]\right)\mathbf{e}_{ij}\mathbf{v}_{ij} + \sum_j C_{ij}\mathrm{d}V_{ij} \tag{38}$$

Details for the coefficients in the SDPD model equations are given in Espanol and Revenga (2003),[30]

2.1 **SDPD Computational Implementation**

The SDPD model has been implemented in a serial version of a code shown in Figure 19. The implementation has the capability of handling complex geometries. The integration scheme for the equation of SDPD particle motion (33) is the modified velocity-Verlet scheme (Groot and Warren, 1997)[32] where the dissipative force component is calculated in two steps for each integration cycle.

Periodic and solid wall boundary conditions have been implemented into the code. The entropy equation has also been implemented and undergone preliminary validations.

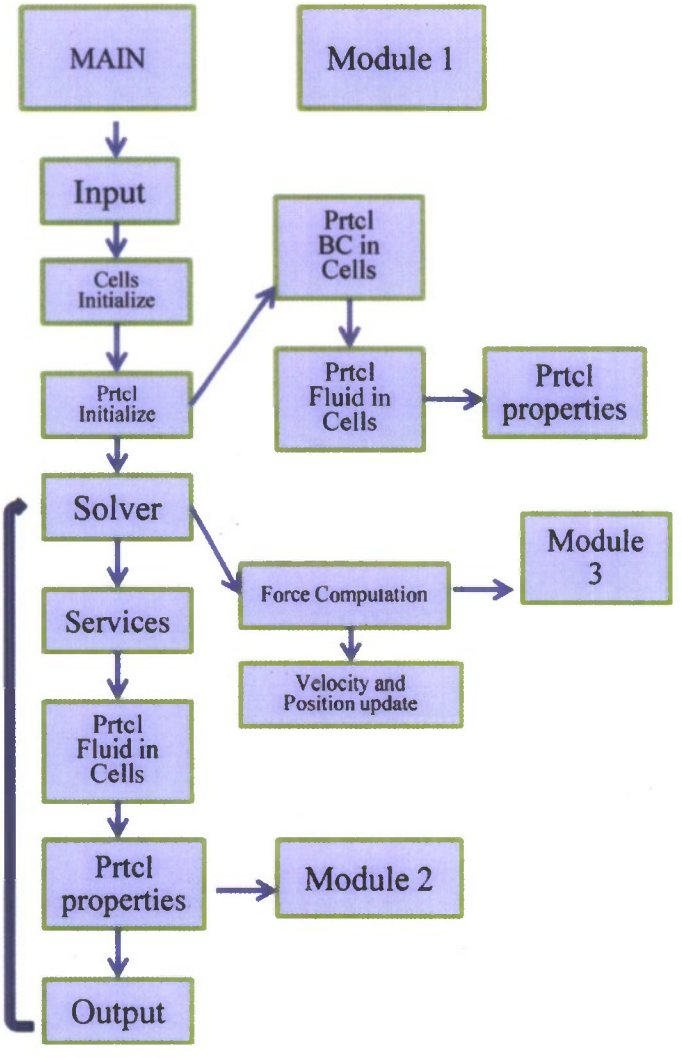

Figure 19. The overall flowchart of the SDPD code.

2.2 Solid Wall Boundary Conditions

The implementation of solid wall boundary conditions in DPD methods is an active research area (Fedosov et al, 2009).[33] We developed under this grant an SDPD approach to represent the geometry of a solid wall. In our model the solid-wall is represented by SDPD particles with positions. The solid-wall SDPD particle velocity is chosen to be opposite in sign and having the same magnitude as the interacting fluid particle velocity. In the current implementation of SDPD the solid-wall particle does not affect the properties of the neighboring fluid particle but does affect the acting force. In our model, the force of the solid-wall and fluid particles is "strong enough" to avoid penetration of fluid par-

ticles inside the wall without the need of arbitrary constants as has been the case of DPD implementations. The algorithmic steps are summarized below and the geometrical characteristics are shown in Figure 20 .

A conservative force component is computed first:

S-1. Compute the conservative force $\mathbf{F}_i^C$ acting on particle i from its neighbor fluid particles contained in its finite support h

S-2. Compute the i particle-wall unit vector $\hat{\mathbf{e}}$

S-3. Compute the projection of the conservative force from step 1) on direction $\hat{\mathbf{e}}$

S-4. If the projected force from $\mathbf{F}_i^C$ is directed towards the wall then apply this contribution to the i-th particle, $\mathbf{F}_W^{C1} = \left(\hat{\mathbf{e}} \cdot \mathbf{F}_i^C\right)\hat{\mathbf{e}}$

A dynamic force component is computed next:

S-1. Compute the fluid velocity component $\mathbf{V}_i^N$ along direction $\hat{\mathbf{e}}$

S-2. Assume that at the wall $\mathbf{V}_W^N = 0$

S-3. Compute the dynamic component for the total force as function of the module of the normal velocity component, $\mathbf{F}_W^{C2} = \dfrac{m_i \Delta V_i^N}{\Delta t}\hat{\mathbf{e}}$

S-4. If the normal velocity component is directed towards the wall then apply this contribution to the i-th particle

S-5. Force on the i-th particle from the wall is $\mathbf{F}_i^C = \mathbf{F}_w^{C1} + \mathbf{F}_w^{C2}$

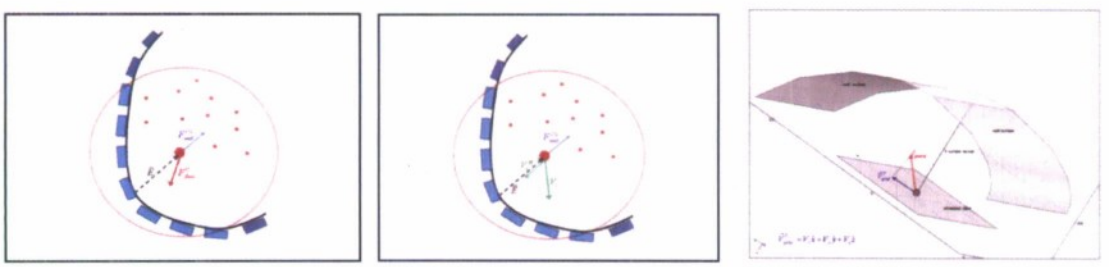

Figure 20. Solid wall implementation in SDPD.

Compute a dissipative force component for the i-th particle:

S-1. For a defined distance Calculate within a defined distance from the wall compute the velocity component $\mathbf{V}_i^T$ normal to $\hat{\mathbf{e}}$ (tangential to the wall)

S-2. Assume that at the wall $\mathbf{V}_w^T = 0$

S-3. Compute the force due to $\mathbf{V}_i^T$ given by $\mathbf{F}_i^D = -m_i \dfrac{\Delta \mathbf{V}_i^T}{\Delta t}$ and apply to the particle.

2.3 Validation of the SDPD Method

The objective of this simulation was to validate the 3D SDPD code as well as the solid-wall boundary condition approach. An incompressible flow was considered in a microchannel with circular constant section of radius 9 microns and length of 20 microns. The fluid simulated is air with viscosity of $\eta = 10^{-6} Kg / ms$, temperature $T = 288^{\circ} K$, density of $0.76 Kg / m^3$ and a Reynolds number of 50. The total number of simulate SDPD fluid particles was 6561 which implies for the given fluid a coarsening factor $N_m \sim 10^7$ and a total Knudsen number of $K_n \sim 10^{-2}$. The flow was driven by imposing an external force acting on each SDPD fluid particle. Frozen SDPD particles, with assigned position, were used to represent the solid wall of the microchannel. Periodic conditions were assigned at the ends of the channel.

Figure 21 shows the axial velocity from SDPD along with the analytical solution for Poiseuille flow. Results show very good agreement between the two profiles.

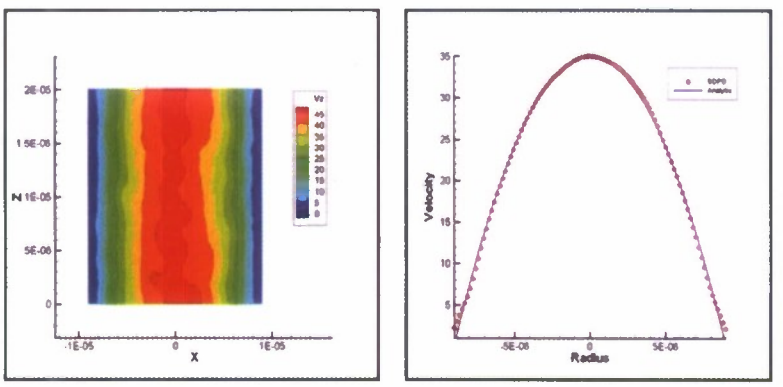

Figure 21. Axial velocity from SDPD and comparison with analytical Poiseuille profile.

A common issue integrating the particle equation of motion for mesoscopic dynamics is the exhibit of nonphysical behavior such as the systematic drift in temperature (for isothermal cases). In order to control the quality of the integration scheme the averaged kinetic energy was monitored as shown in Figure 22. The results display the good convergence and small level of fluctuations of our SDPD implementation. The density across the microchannel shown in Figure 22 has a fractional fluctuation of less than 0.22% and demonstrates the ability of the solid-wall boundary condition developed in this work.

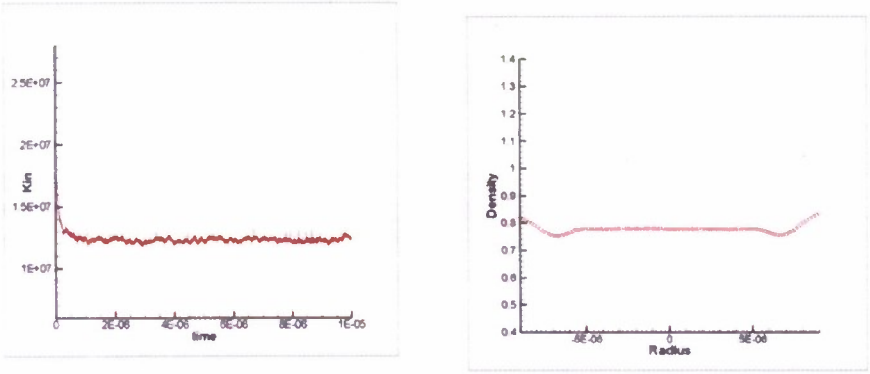

Figure 22. Average kinetic energy as a function of time and density across the channel from the SDPD simulation.

A second simulation example involved a fluid in a periodic domain with given temperatures and random velocities. The entropy equation (37)was included in the simulation with the heat transfer term shown in eq. (37). The simulation was run for about 500 timesteps.

Figure 22 shows the entropy and average SDPD particle temperature in the domain. The increase in entropy and the average temperature is due to the irreversibility of the heat transfer term in the entropy equation. The simulation shows that equilibration is maintained without any unphysical increase in temperature.

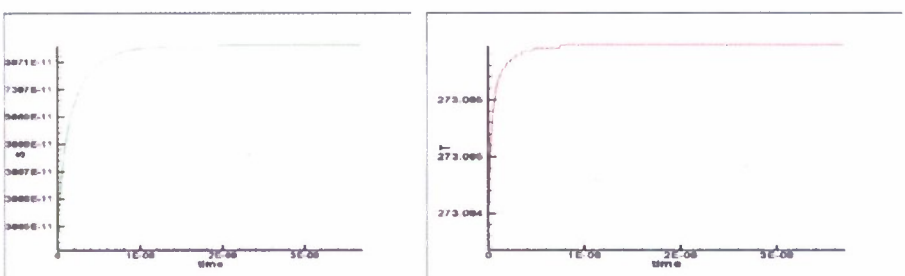

Figure 23. Entropy and average temperature from SDPD simulation.

2.4 **Conclusions**

We implemented successfully the SDPD method, a thermodynamically consistent DPD model. We developed a boundary condition methodology that does not require arbitrary constants. The method and code have been validated successfully for isothermal pressure driven flows. Simulations of non-isothermal flows exhibited good convergence properties.

3 PERSONNEL SUPPORTED

The following personnel were partially supported during the period of performance of this grant. The educational status at the time of their support as well as their current position is also indicated.

1. Dr. N. A. Gatsonis, PI, Professor of Mechanical Engineering.
2. Pawel Wroblewski, Visiting International Scholar.
3. Ryan Chamberlin, Ph.D. Candidate. Current Position: Research Engineer, Alion Science and Technology, Middletown, RI.
4. Anton Spirkin, Post Doctoral Fellow. Current Position: Senior Research Engineer, Technical Software Development, Exxon, Houston, TX.
5. Wael Al-Kouz, Ph.D. Candidate. Current position: Senior Mechanical Engineer, Fairbanks Mechanical Contractors, Fairbanks, AL.
6. Raffaele Potami, Post Doctoral Fellow. Current Position: Post Doctoral Fellow, WPI.
7. Nick Behlman, M.S. Candidate. Current Position: M.S. Candidate.

4 PUBLICATIONS

The following publications related to this research appeared during the period of performance of the grant.

4.1 Journal and Conference Proceedings:

1. Gatsonis, N.A. and A. Spirkin, "A Three-dimensional Electrostatic Particle-in-Cell Methodology on Unstructured Delaunay-Voronoi Grids", *Journal of Computational Physics*, Volume 228, Issue 10, 1 June 2009, Pages 3742-37613, 2009.
2. Chamberlin, R. E., and Gatsonis, N. A., "Numerical Modeling of Gas Expansion from Microtubes," *Journal of Nanoscale and Microscale Thermophysical Engineering*, Vol. 12, No. 2, pp. 170-185, 2008.
3. Chamberlin, R.E., and Gatsonis, N.A., "Numerical Modeling of Gaseous Expansion from Micro and Nanonozzles," *Rarefied Gas Dynamics*, edited by A. Rebrov and M. Ivanov, 2007.
4. Gatsonis, N. A., Al Kouz, W. G., and Chamberlin, R. E, "Scale Effects on Rarefied Supersonic Flows in Nanochannels", ICNMM2008-62274, Proc. of the 6th ASME International Conference on Nanochannels, Microchannels and Minichannels, Frankfurt, Germany, June 2008.
5. Chamberlin, R. E., and Gatsonis, N. A., "Numerical Modeling of Gas Expansion From Microtubes," CNMM2006-96120, Proc. of the 4th ASME International Conference on Nanochannels, Microchannels and Minichannels, Limerick, Ireland, June 2006.

6. Chamberlin, R. E., and Gatsonis, N. A., "DSMC Simulation of Microjet Expansion and the Design of a Micro Pitot Probe," AIAA- 2006 379, 9th AIAA Joint Thermophysics and Heat Transfer Conference, San Francisco, CA, June 2006.

4.2 Dissertations

1. Chamberlin, R., "*A three dimensional Direct Simulation Monte Carlo Methodology on Unstructured Delaunay Grids with Applications to Micro and Nano flows*," PhD. Dissertation, March 2007.
2. Al-Khouz, W., "*Investigation of Supersonic Gaseous Flows into Nanochannels using a 3D Unstructured Direct Simulation Monte Carlo Method*", Ph.D. Dissertation, WPI, Worcester, June 2009.

6. REFERENCES

[1] Gatsonis, N.A. and A. Spirkin, "A Three-dimensional Electrostatic Particle-in-Cell Methodology on Unstructured Delaunay-Voronoi Grids", Journal of Computational Physics, 3/2009.

[2] Chamberlin, R., *A three dimensional direct simulation Monte Carlo methodology on unstructured Delaunay grids with applications to micro and nano flows*, PhD. Dissertation, March 2007.

[3] Al-Khouz, W., "*Investigation of Supersonic Gaseous Flows into Nanochannels using a 3D Unstructured Direct Simulation Monte Carlo Method*", Ph.D., WPI, Worcester, June 2009.

[4] Gatsonis, N. A., Al Kouz, W. G., and Chamberlin, R. E, "Scale Effects on Rarefied Supersonic Flows in Nanochannels", ICNMM2008-62274, Proc. of the 6th ASME International Conference on Nanochannels, Microchannels and Minichannels, Frankfurt, Germany, June 2008.

[5] Chamberlin, R.E., and Gatsonis, N.A., "Numerical Modeling of Gaseous Expansion from Micro and Nanonozzles," *Rarefied Gas Dynamics*, edited by A. Rebrov and M. Ivanov, 2007.

[6] Chamberlin, R. E., and Gatsonis, N. A., "Numerical Modeling of Gas Expansion from Microtubes," *Journal of Nanoscale and Microscale Thermophysical Engineering*, Vol. 12, No. 2, pp. 170-185, 2008.

[7] Hadjiconstantinou, N. G., Garcia, A. L., Bazant, M. Z., and He, G., "Statistical error in particle simulations of hydrodynamic phenomena," *Journal of Computational Physics.*, Vol. 187, 2003, pp. 274-297.

[8] Bird, G. A., *Molecular Gas Dynamics and the Direct Simulation of Gas Flows*, Oxford University Press, Oxford, 1996.

[9] Borgnakke, C. and Larsen, P. S., "Statistical collision model for Monte Carlo simulation of polyatomic gas mixture," *J. Comp. Phys.*, **18**, pp. 405-420, 1975.

[10] Nance, R., Hash, D., and Hassan, H., "Role of Boundary Conditions in Monte Carlo Simulations of MEMS Devices," *Proc. of the 35th Aerospace Sciences Meeting and Exhibit*, Reno, NV, 1997.

[11] Liou, W. and Fang, Y. "Implicit Boundary Conditions for Direct Simulation Monte Carlo Methods in MEMS Flow Predictions," *CMES*, Vol. 1, 2000, pp. 119-128.

[12] Wang, M. and Li, Z. "Simulations for gas flows in microgeometries using the direct simulation Monte Carlo method," *Int. Journal of Heat and Fluid Flow*, Vol. 25, 2004, pp. 975-985.

[13] Hirsch, C. Numerical Computation of Internal and External Flows, Volume 2, Wiley, 1990

[14] Yee, H. C., Beam, R. M. and Warming, R. F., "Boundary Approximations for Implicit Schemes for One-Dimensional Inviscid Equations of Gasdynamics," *AIAA Journal*, Vol. 20, No. 9, pp. 1203-1211, 1982.

[15] Liou, W. W., Fang, Y.C., "Heat transfer in microchannel devices using DSMC," *Microelectromechanical systems*, 10-2, pp. 274-279, 2001.

[16] Le, M., Hassan, I., Esmail, E., "The effects of outlet boundary conditions on simulating supersonic microchannel flows using DSMC", *Applied Thermal Engineering* 27, pp. 21-30, 2007.

[17] Hadjiconstantinou, N. G., "Analysis of discretization in the direct simulation Monte Carlo," *Phys. Fluids*, **12**(10), pp. 2634-2638, 2000.

[18] G. A. Bird, M. A. Gallis, J. R. Torczynski, and D. J. Rader, Accuracy and efficiency of the sophisticated direct simulation Monte Carlo algorithm for simulating noncontinuum gasflows, Phys. Fluids 21, 017103, 2009.

[19] Karniadakis, G., Beskok, A., and Aluru, N., Microflows and Nanoflows, Springer, 2005.

[20] Liou, W. W. and Fang, Y, *Microfluid Mechanics*, McGraw-Hill, New York, 2006.

[21] Hughes, P. C. and de Leeuw, J. H., "Theory for the Free Molecule Impact Probe at an Angle of Attack," *Rarefied Gas Dynamics*, Vol. 1, Academic Press, New York, 1965, pp. 653-676.

[22] Moss, J. N., and Bird, G.A., "Monte Carlo Simulations in Support of the Shuttle Upper Atmospheric Mass Spectrometer Experiment," *Journal of Thermophysics*, Vol. 2, No. 2, 1988, pp. 138-144.

[23] Kannenberg, K. C., and Boyd, I. D., "Monte Carlo Computation of Rarefied Supersonic Flow into a Pitot Probe," *AIAA Journal*, Vol. 34, No. 1, 1994, pp. 83-88.

[24] Gatsonis, N. A., Maynard, E., and Erlandson, R. E., "Monte Carlo Modeling and Analysis of Pressure Sensor Measurements During Suborbital Flight," *Journal of Spacecraft and Rockets*, Vol. 34, No. 1, pp. 83-91, 1997.

[25] Oh, C.K., Oran, E.S., Sinkovits, R.S., Computations of high-speed, high Knudsen number microchannel flows, *Thermophysics and Heat Transfer*, 11-4, pp. 497-505, 1997.

[26] Mavriplis, C., Ahm, J. C., Goulard, R., Heat transfer and flow fields in short microchannels using direct simulation Monte Carlo, *Thermophysics and heat transfer*, 11-4,pp. 489-496,1997.

[27] Le, M., Hassan, I., "Simulation of heat transfer in high speed microflows", *Applied Thermal Engineering* 26,pp. 2035-2044, 2006 .

[28] Alexander, F. J., Garcia, A. L., and Alder, B. J., "Cell size dependence of transport coefficients in stochastic particle algorithms," *Phys. Fluids*, **10** (6), pp. 1540-1542, 1998.

[29] Wilmoth, R.G., Dogra, V. K., and Moss, J. N., "Energetics of Gas-Surface Interactions in Transitional Flows at Entry Velocities," *Journal of Spacecraft and Rockets*, Vol. 29, No. 6, 1992, pp. 786-793.

[30] Espanol, P. and Revenga, M. Smoothed Dissipative Particle Dynamics. Physical Review, 2003, Vol. 67.

[31] Liu G.R. and Liu, M.B. *Smoothed Particle Hydrodynamics a meshfree particle method.* World Scientific Printers, Singapore, 2003.

[32] Groot, R. and Warren, P. Dissipative particle dynamics: Bridging the gap between atomistic and mesoscopic simulation, J. Chem. Phys. 107, 4423–4435 (1997).

[33] Fedosov,D., I. Pivkin, G. Karniadakis. Velocity limit in DPD simulations of wall-bouded flows. Journal of Computational Physics. 2008, Vol. 227.